Chapter 2

IN-VIVO DISTINCTION BETWEEN PLASMA MEMBRANE AND NEAR-MEMBRANE ORGANELLES USING VARIABLE ANGLE TOTAL INTERNAL REFLECTION FLUORESCENCE MICROSCOPY (VA-TIRFM)

We have optically sectioned living cells to a maximum depth of ~250 nm using a Variable Angle-Total Internal Reflection Fluorescence Microscope (VA-TIRFM). This yields 3D images of cell membranes and nearby organelles similar to that gained by confocal microscopes but with at least an order-of-magnitude greater z resolution. It also enables cellular membranes to be imaged in near isolation from cell organelles. Key to achieving this resolution was integration of a controllable excitation laser micropositioner into a standard through-the-lens TIRF illuminator and development of a custom culture dish for re-use of expensive high index of refraction cover slips. Images are acquired at several penetration depths by varying the excitation laser illumination angles. At the shallowest penetration depth (~46 nm) just the membrane and a few internal puncta are imaged. As the penetration depth is increased up to 250 nm organelles near the membrane, such as the ER, are imaged as well. The sequence of images from shallow deep is processed to yield a z-stack of images of approximately constant thickness at increasing distance from the coverslip. We employ this method to distinguish membrane-localized fluorophores (α4 GFP β2 nicotinic acetylcholine receptors and pCS2:lyn-mCherry) at the plasma membrane (PM) from those in near-PM endoplasmic reticulum (ERTracker green, α4 GFP β2 nicotinic acetylcholine receptors), on a z-axis distance scale of ~45 to ~250 nm in N2a cells. In doing so we observe occasional smooth ER structures that cannot be resolved as being distinct from the membrane.

2.1 Variable Angle Total Internal Reflection Fluorescence Microscopy overview

Total Internal Reflection Fluorescence Microscopy (TIRFM)[1] is a widely used technique for imaging cellular structure near a membrane that is adhered to a thin glass coverslip. This technique takes advantage of a basic principal of optics: the angle of refraction will be greater than the angle of incidence when light reaches an interface where the transport

media sharply changes from a higher to a lower index of refraction. The relationship between these angles is a function of the index of refraction of the two materials as described by Snell's law,

$$n_1 \sin\theta_1 = n_2 \sin\theta_2$$

where θ_1 is the angle of incidence and θ_2 is the angle of refraction for two materials with indexes of refraction n_1 and n_2 as seen in Figure 2.1.

When the angle of refraction is $\geq 90°$ light can no longer cross the material boundary and is reflected from the interface with the lower index of refraction material back into the higher index of refraction material. This can be described as a total internal reflection. The minimum angle at which total internal reflection occurs is called the critical angle. Snell's law can be readily solved for this critical angle:

$$\theta_c = \sin^{-1}(n_2 / n_1)$$

An evanescent field is generated on the lower index of refraction side of this interface. The

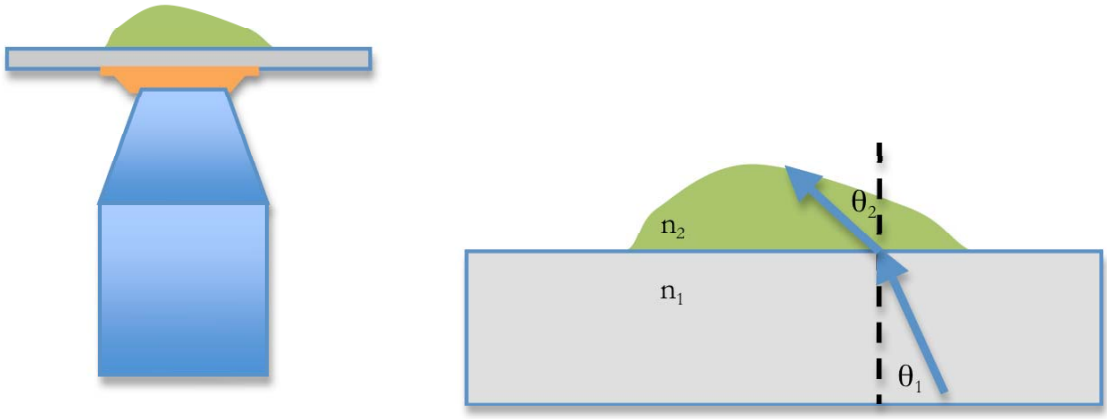

Figure 2.1. An epifluorescence microscope was used in this study. In this type of microscope the objective is under the sample as seen on theleft side of this figure. Immersion oil is used to match the index of refraction of the coverslip. The sample is on top of the coverslip. In objective-based TIRF the excitation laser is focused on the outside edge of the back aperture of the objective. The angle at which the excitation laser light emerges from the objective is determined by the radial positon of the focused excitation beam on the back aperture. θ_1 and θ_2 describe the angle of the excitation laser within the coverslip and in the sample. The index of refraction of the coverslip and the sample are described by n_1 and n_2.

intensity of that evanescent field decays exponentially with distance, z, from the transport media interface as described by

$$I(z) = I(0)e^{-z/d}$$

Where, for surface polarized illumination, the intensity of the evanescent field at the interface

$$I(0) = \frac{4\cos^2\theta}{1-(\frac{n_2}{n_1})^2}$$

The penetration depth of the evanescent field,

$$d = \frac{\lambda}{4\pi n_1}(\sin^2\theta - \sin^2\theta_c)^{-1/2} = \frac{\lambda}{4\pi}(n_1{}^2\sin^2\theta - n_2{}^2)^{-1/2},$$

is defined by the specifics of the situation: the wavelength of the light, the transport media indexes of refraction and the degree to which the angle of incidence exceeds the critical angle. Note that for a given wavelength of light and set of transport media the penetration depth varies considerably. The penetration depth describes the depth at which the evanescent field intensity has decayed to 1/e, or approximately 36.8%, of the field strength at the surface.

The penetration depth is minimized when the angle of incidence is much greater than the critical angle. As the angle of incidence is reduced the penetration depth increases. Therefore a series of images taken of a sample at decreasing angle of incidence will show successively deeper sections of the cell even though all of those images are total internal reflection images. In other words: by controlling the excitation laser angle the thickness of the cell region being imaged can be varied.

This is the basis for the technique called Variable Angle-Total Internal Reflection Fluorescence Microscopy[2] (VA-TIRFM). Since Lanni, Waggoner and Taylor's pioneering work the theory has been expanded, as have the concepts for processing the data. In the

process of advancing VA-TIRFM techniques exploratory studies have been conducted to characterize cell-surface contact topology[2,3,4], image cellular focal adhesion sites[5], determine secretory vesicle motion in 3 dimensions[6,7,8], measure protein and polymer film thickness[9], solute depth dependent concentration profiles[10,11] and determine the length of λ-DNA strands.[12]

These exploratory studies successfully confirmed the theory developed for VA-TIRFM data analysis and refined instrument concepts. They also demonstrated the potential utility of this technique for studying cellular events near the membrane.

However no significant scientific insights have been derived through application of VA-TIRFM, nor has it become widely utilized in studies despite the proliferation of TIRF capable microscopes. Why has the promise yielded so little?

Unfortunately the efficacy of VA-TIRFM was severely limited by the numerical aperture of available objectives. The numerical aperture (NA) can be used to describe the maximum angle of incidence light that can be transmitted through transport media, such as a coverslip, by a microscope objective. Specifically:

$$\theta_{\max} = \sin^{-1}\frac{n_1}{NA}$$

A given microscope objective can be used for objective based TIRF if $\theta_{max} \geq \theta_c$. In other words a microscope objective can only be used for objective based TIRF if $NA > n_2$. Consider a sample with index of refraction n_2 on a coverslip with index of refraction n_1. A microscope objective can be used for TIRF imaging a thin sample in air if microscope NA>1. Objective based TIRF can be accomplished with water if its NA>1.33. Cells can barely be imaged in TIRF with a 1.4 NA objective and more commonly require a 1.45 NA objective since the average cellular index of refraction is 1.385.[13]

All four of the major microscope manufacturers have produced objectives with NA's as high as 1.45 since 2005. Unfortunately many cellular organelles have indexes of refraction that approach 1.45 and some that exceed that value. The index of refraction of lysosomes

and melanin even exceeds the 1.52 index of refraction typical of glass coverslips. Table 2.1 presents a list of cellular components and their indexes of refraction.

Cell Component	Index of refraction
Extracellular fluid	1.35–1.36[14]
Cytoplasm	1.36–1.375[15]
Nucleus	1.38–1.41[16]
Mitochondria	1.40[17]
Lipid	1.48[18]
Lysosomes	1.60[19]
Melanin	1.6–1.7[20]

Table 2.1 The index of refraction of several cellular components.

As was seen earlier, confinement of the evanescent field depends significantly on the difference between the index of refraction of the coverslip and that of the specimen. The importance of these observations is demonstrated in Figure 2.2 where it is demonstrated that in a typical TIRF imaging configuration no cellular components with indexes of refraction greater than 1.42 will be in TIRF. Given the highly inhomogeneous nature of cells all that can be confidently claimed is that a cell is TIRF imaged with a 1.45 NA objective over a wide, ill-defined depth that varies across the image depending on the cell's specific characteristics. The penetration depth ranges from ~130 nm for n=1.385 to ∞ for n>1.42 at the extreme outer edge of the objective for a 1° beam width centered in the TIRF range. From there it rapidly degrades should the beam be adjusted closer to the critical angle. It is also clear from Figure 2.2 that the results of previous investigators using VA-TIRM were significantly limited by the index of refraction of glass and the NA of typical TIRF objectives. Hence we can conclude that VA-TIRFM cannot effectively discriminate between cellular components located within about 200 nm of the surface if a glass coverslip and 1.45 NA objective are used.

Olympus also makes an APO 1.65 NA/100x objective. Two barriers have impeded the widespread use of this objective: the 1.8 index of refraction immersion oil is both toxic and unpleasant and the 1.8 index of refraction coverslips cost $40 each. As a result this objective is very rarely used and is still produced only by Olympus.

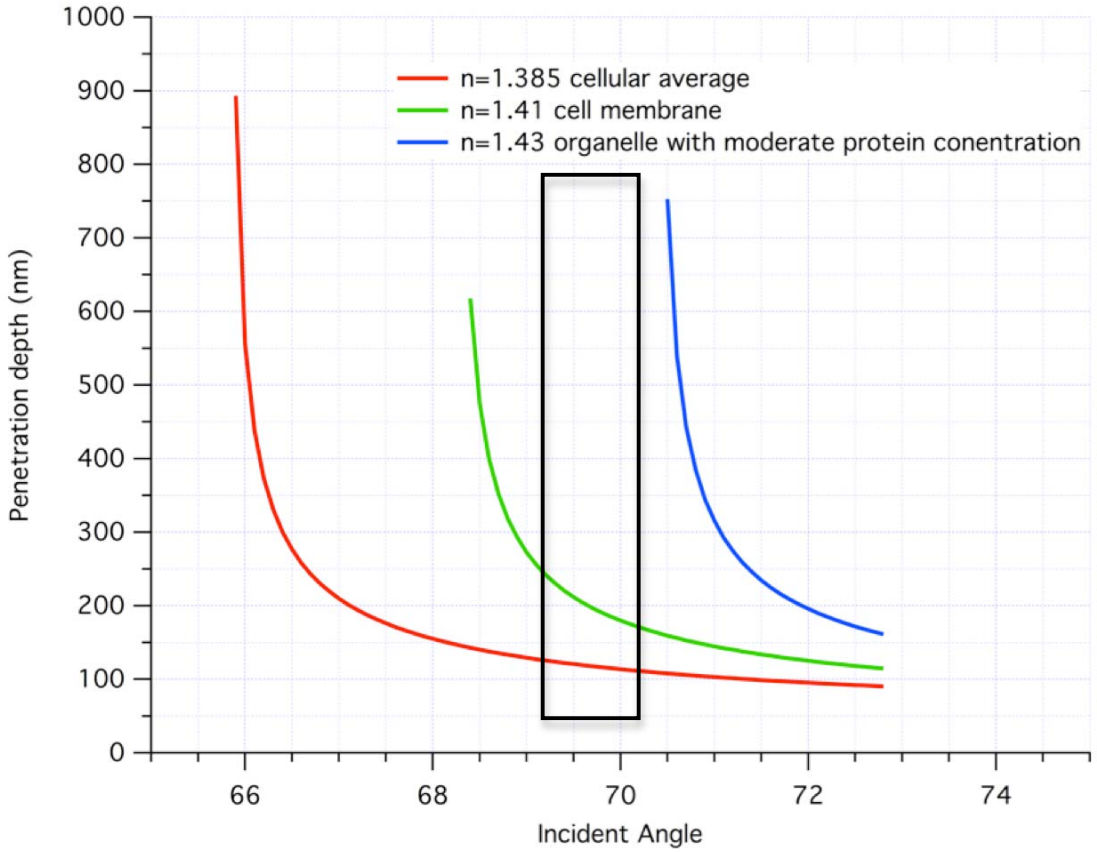

Figure 2.2. A typical TIRF microscope cannot distinguish a cell membrane from its organelles as the cellular indexes of refraction are similar to the 1.45 NA of the microscope objective. As result, the depth TIRF imaged at any given incident angle will vary considerably with cellular structure. The evanescent field penetration depths shown here were calculated for the indexes of refraction of several common cellular organelles. The values presented assume objective-based TIRFM through a 1.45 NA objective with a 488 nm wavelength excitation laser through a glass coverslip. The rectangular box is 1.0° wide and located at the center of the TIRF angular range for this combination.

The penetration depth as a function of angle of incidence and cell component index of refraction are shown in Figure 2.3 for a 1.65 NA objective. These calculations were performed for a 488 nm excitation laser and N-LAF21 coverslip (n=1.7993 at 488 nm)[21]. It is clearly seen that the high index of refraction coverslip results in very tight confinement of the evanescent field. In addition, the variation in the index of refraction of cellular components is small in comparison with the difference between their values and the 1.65 objective's. In combination, the result is that the penetration depth is very shallow and nearly constant across most of the TIRF angular range. Therefore this opens the possibility to vary the incident angle to optically section a cell, and thereby to characterize the fluorescent density as a function of depth.

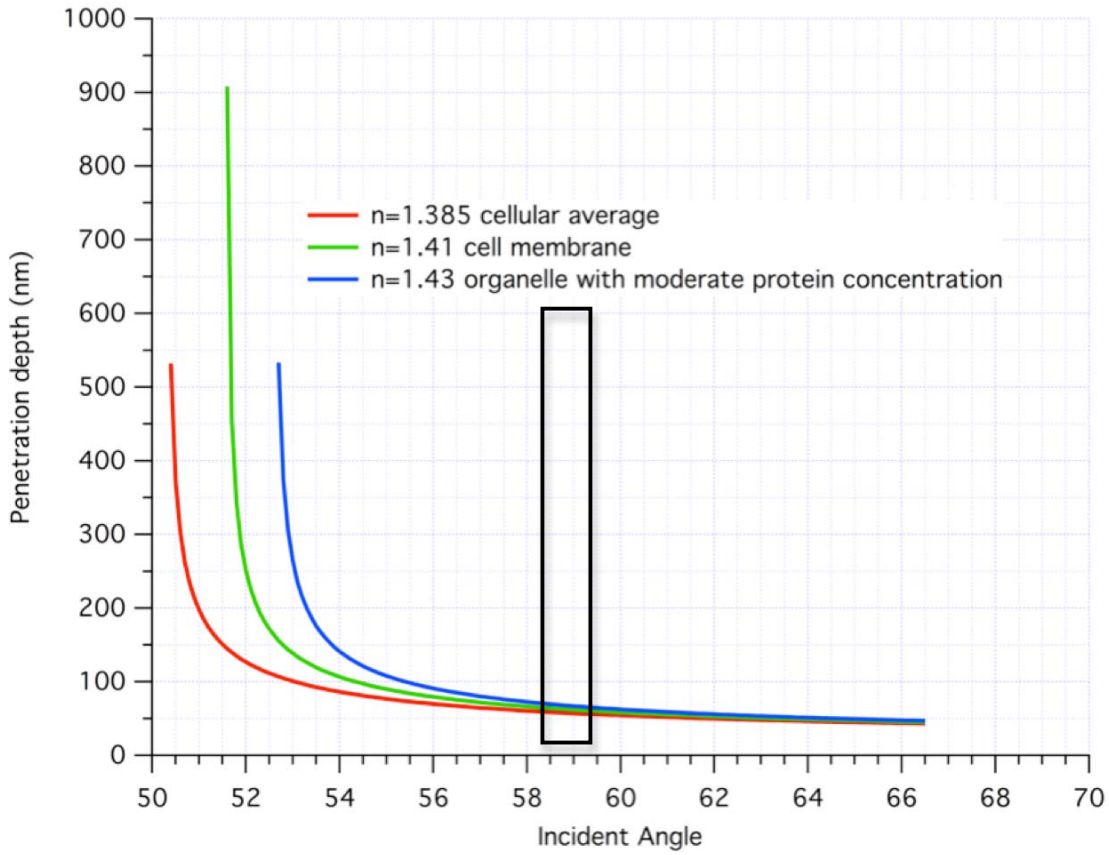

Figure 2.3. A cell can be imaged in pure TIRF (no far field component) with uniform z-thickness, regardless of cellular index of refraction, using a 1.65 objective. Over the boxed range of incident angles, the penetration depth is 60 nm for a 1.385 cellular average index of refraction. There is little difference in penetration depth as a function of cellular component index of refraction. The black rectangular box is 1.0 degree wide and approximates the full width 20% max beam width of our 488 nm excitation laser. The box is centered in the TIRF range for this objective when looking at cells. This figure shows the calculated penetration depth as a function of incident angle and index of refraction for a 1.65 NA objective. These calculations were made for 488 nm laser excitation and assume the use of a N-LAF21 coverslip with an index of refraction of 1.7993 at 488 nm.

In summary: VA-TIRFM is a good idea with a sound, and well-developed, theoretical basis. Initial experiments used 1.45 NA microscope objectives that did not permit sufficient discrimination in z for this approach to provide new insights. However, we demonstrate here that useful VA-TIRFM becomes a real possibility with a 1.65 NA objective and n≅1.8 coverslips.

2.2 VA-TIRFM image processing

One of the most carefully considered VA-TIRFM image processing techniques is the

inverse Laplace transform.[22,23,24] Recall that the intensity of the evanescent field in z is described by

$I(z) = I(0)e^{-z/d}$ where z is the distance to the coverslip surface, d is the penetration depth and the evanescent field intensity at the coverslip surface is

$$I(0) = \frac{4\cos^2\theta}{1-(\frac{n_2}{n_1})^2}$$ for s-polarized excitation.

The product of the distribution of fluorophore concentration in z with the variation in fluorophore collection efficiency with z can be described by $D(z)$.[25] Then the measured fluorescence for a given $D(z)$, assuming that the brightness of a given fluorophore is only a function of the evanescent field intensity and the distance from the fluorophore to the coverslip surface, is

$$F(\theta) = I(0,\theta)\int_0^\infty D(z)e^{-z/d(\theta)}dz.$$

Extending this to describe a two dimensional surface, the z distribution of fluorophores is

$$F_{x,y}(\theta) = I_{x,y}(0,\theta)\int_0^\infty D_{x,y}(z)e^{-z/d(\theta)}dz.$$

Also recall that a Laplace transform of a function $f(t)$ is formally defined as

$$F(s) = \int_0^\infty f(t)e^{-st}dt$$

Then the expression that describes $F_{x,y}(\theta)$ is the Laplace transform of $D_{x,y}(z)$.

As $F_{x,y}(\theta)$ is the Laplace transform of $D_{x,y}(z)$ it is reasonable to attempt to use the inverse Laplace transform of $F_{x,y}(\theta)$ to solve for $D_{x,y}(z)$. This approach assumes that the evanescent field intensity is both constant and uniform over the x-y plane. It also assumes

that the field distribution over x-y is uniform and only varies with θ as described above. Successful application of an inverse Laplace transform on appropriate VA-TIRFM data would enable complete deconvolution of the three-dimensional distribution of fluorophore concentration.

Unfortunately the TIRFM that we used for this experiment evidences a very significant interference pattern across the coverslip that changes sharply with angle. The resulting variation in evanescent field intensity makes the inverse Laplace transform approach to reconstructing the continuous 3D profile of fluorophore concentration challenging.

We note that the variation in field due to the interference pattern is small compared with that caused by large changes in incident angle. Such large changes in incident angle also result in large changes in penetration depth as the critical angle is approached. In other words: the signal-to-noise ratio is significantly improved when images of significantly different penetration depth are differenced instead of using finely incremented images.

The theory above suggested a novel and relatively simple method for 3D image reconstruction using VA-TIRFM: treat the difference between a series of images taken with increasing penetration depth as being representative of the cell structure as function of depth. This approach formed the basis for the work presented in this chapter.

If the difference in the evanescent field strength at the coverslip, I(0), is accounted for sequential images can be directly compared. As an example, with the excitation beam closest to the maximum angle, an approximately 45 nm thick image of the cell is captured. Another image can be taken closer to the critical angle such that the penetration depth is increased to 90 nm. These images can be multiplied by a normalization factor that accounts for the change in evanescent field intensity. By subtracting the first image from the second after normalization, a pair of optically sectioned images is obtained: each of which is ~45 nm thick.

Here we chose to discriminate cellular structure in z by analyzing the difference between images taken at five different angles ranging from the something very close to the critical

angle to something very close to the maximum angle of the 1.65 NA objective was. Surprisingly this simple approach to 3D image reconstruction has not been previously reported

In Figure 2.4 an example of optical sectioning is presented in which a sequence of images is captured at several angles of incidence. The first image primarily shows the 48 nm closest to the coverslip. A second image is taken at a penetration depth of 72 nm. This second image can be considered to contain all of that information found in image 1, plus

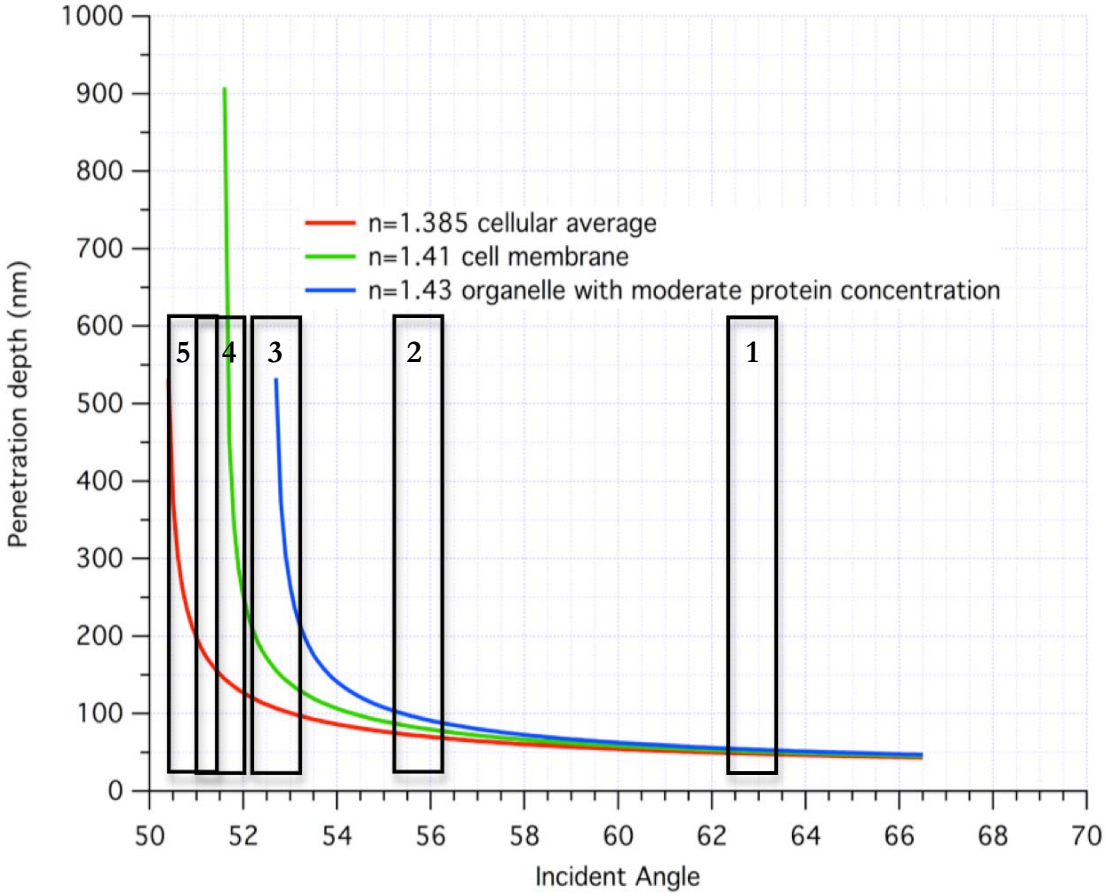

Figure 2.4. A five image VA-TIRFM sequence is shown relative to cellular organelle indexes of refraction. The five black rectangular boxes each represent an image in this sequence. Optical sectioning is achieved by choosing excitation laser incident angles such that the average penetration depth of each successive image is 1.5 times that of the previous one (Table 5.3). The image boxes are 1.0 degree wide and match the full width 20% max beam width of our 488 nm excitation laser. The 5th image (far left box) is centered on a penetration depth of 243 nm for a cell's average index of refraction (1.385). Because of the beam width this image includes incident angles that result in penetration depths ranging between 160 nm up to ~700 nm. That real beam size effectively limits the center penetration depth to ~250 nm for a pure TIRF image (no far-field content). The calculations shown above assume a 1.65 NA objective, 488 nm laser excitation and the use of a N-LAF21 coverslip with an index of refraction of 1.7993 at 488 nm.

that of the next 24 nm. Several of these differenced images can be used to build a 3 dimensional image of the 250 nm closest to the coverslip. In doing so the fluorescent content of the membrane is largely isolated from the fluorescent content of the Endoplasmic Reticulum (ER) and other cellular organelles close to the membrane.

The width of the focused excitation laser beam on the back aperture of the objective was measured and found to be ~42 microns (full width at 20% max height) or about 1° in terms of the incident angle variation near the critical angle. Therefore the width of the boxes shown in Figure 2.4 represent a 1° beam width. The penetration depth is seen to range from ~700 nm to 160 nm across a 1° wide box centered at 50.8° incidence angle for cell with an average index of refraction of 1.385 adhered to a coverslip with an index of refraction of 1.7993. The penetration depth is 240 nm at the center of the box.

We conclude from this that a single image, containing only TIRF and no far-field illumination, has a practical depth limit of about 250 nm using this specified microscope. However we noted that a difference image, produced by subtracting an image taken at a somewhat greater incident angle from one taken proximate to the critical angle, and show detail at depths greater than 250 nm while still being in TIRF.

What image sequence should be selected? Since we have measured the variation in field intensity with angle, and can use those values to normalize, it is not an important factor in selecting the specific angles for the image sequence. The two most important factors are penetration depth and field intensity.

The integrated evanescent field at any incident angle is

$$\int_0^\infty I(z)dz = \int_0^\infty I(0)e^{-z/d}dz = I(0)\int_0^\infty e^{-z/d}dz = I(0)(d)$$

Consider the integrated field intensity ratio between images taken at two angles such that $d_2 = 2d_1$. We have already noted that normalization is done to account for the change in evanescent field intensity $I(0)$ with the change in incident angle. Therefore the

Integrated intensity angle 1/angle 2= $\frac{I(0)d_1}{I(0)d_2} = \frac{d_1}{2d_1} = \frac{1}{2}$

We see that the integrated field intensity is directly proportional to penetration depth once the field intensity at the surface as a function of angle has been normalized! Twice the penetration depth results in twice the normalized integrated evanescent field intensity.

To implement this technique the relationship between beam position, as measured by the closed-loop controller, and the incident angle of the excitation beam in the coverslip was determined. We also determined the actual variation in evanescent field strength as a function of beam position. Using this information we can then choose which incident angles to image knowing the penetration depth at each location. The calibrations were also used to appropriately normalize the measured intensity of the field strength and thereby to enable to direct image differentiation.

In Appendix A we present the details of the critical calibrations that were used to define and normalize the image sequence. These calibrations include the measured relationships between the excitation beam position and excitation beam angle of incidence. Also presented in Appendix A is the measured field intensity as a function of angle (and beam position) at the coverslip surface. This is compared with the field variation with incident angle predicted by theory. We find that the surface evanescent field intensity was approximately 10% less than that predicted by theory over the TIRF range of incident angles. At present we can only speculate as to the origin of this discrepancy. One possibility is that the evanescent field intensity is diminished across the coverslip in the direction of propagation due to scattering caused by the sample and coverslip surface roughness. An alternative explanation is that the difference is due to my measurement and/or data analysis error. A third is that a small fraction of the excitation energy within the evanescent region might contain some vertically polarized energy.

Using these calibrations, difference processing a stack of images taken at different incident angles is straightforward. As an example: having taken an image at each of five incident angles, the background is then subtracted from each. The field intensity variation with angle at the surface can be readily normalized since we have measured this. Then each

image is multiplied by a normalization factor to account for the change in field intensity with angle. Then image 1 is subtracted from image 2. Image 2 is subtracted from image 3. Image 3 is subtracted from image 4. And finally Image 4 is subtracted from image 5. ImageJ v1.44c[26] was used to perform the image processing steps involved in producing the results presented in this thesis.

The resulting stack of images includes the section nearest the coverslip, the section just above this and so on. This information contained in this group of images is analogous to a z-stack of images taken by a confocal microscope albeit with much finer z-axis resolution. This image stack can then be viewed as a three dimensional image using ImageJ or a variety of other programs. All of the 3D visualizations presented in this thesis were created using Imaris 7.0[27] in the Beckman Imaging Center at Caltech.

Since the normalized integrated field intensity is directly proportional to penetration depth, the most obvious imaging sequence strategy is to use even steps in penetration depth. The shallowest section is 48 nm. Therefore in Table 2.2 an imaging sequence is described where the penetration depth of each image is incremented by 48 nm. This approach enables a 5 slice image to be acquired with the deepest slice having a 240 nm penetration depth.

Image number	Penetration depth	Δ depth	Incident angle
1	48 nm	48 nm	63°
2	96 nm	48 nm	53.3°
3	144 nm	48 nm	51.6°
4	192 nm	48 nm	51.1°
5	240 nm	48 nm	50.9°

Table 2.2 Five image sequence with each image being the same thickness.

Another reasonable approach would be to image in even logarithmic steps so that an even multiple of energy is contained in the sequential images after normalization for the chance in z=0 evanescent field strength. An alternate approach is to choose incident angles so that the thickness change is constant through the sequence. Post-normalization sequential image subtraction produces a differential image in the axial direction.

Table 2.3 shows the parameters for a logarithmic sequence in which five successive images contain 1.5 times as much energy (same thing as saying 1.5 times the penetration depth) as the previous image did after normalization.

Image number	Penetration depth	Δ depth	Incident angle
1	48 nm	48 nm	63°
2	72 nm	24 nm	55.7°
3	108 nm	36 nm	52.7°
4	162 nm	54 nm	51.4°
5	243 nm	81 nm	50.9°

Table 2.3 Five image sequence-logarithmic. Each image has 1.5 times the penetration depth of the previous one. This sequence is also shown in Figure 2.4.

For both of the idealized solutions just discussed, noise is an issue. Camera noise, light leakage throughout the path, secondary reflection induced interference of excitation beam, non-uniformity of excitation beam due to alignment errors, laser intensity fluctuation, photobleaching are all concerns. Paucity of signal (photon starvation) is always a concern as well. The differencing technique we propose to use for VA-TIRFM image processing is less sensitive to some of these issues than most direct imaging techniques (e.g. background noise is exactly subtracted out from successive images along with the shallower TIRF information).

Sources of error that change between images are particularly troubling. As noted earlier, the most significant of these appears to be variation of the excitation field intensity due to interference. Such interference between the main excitation beam and reflections within the optical path could be caused by misalignment, non-ideal optical anti-reflection coatings and immersion oil mismatch of index of refraction. The effect of laser interference on differenced images is seen in Figure 2.5.

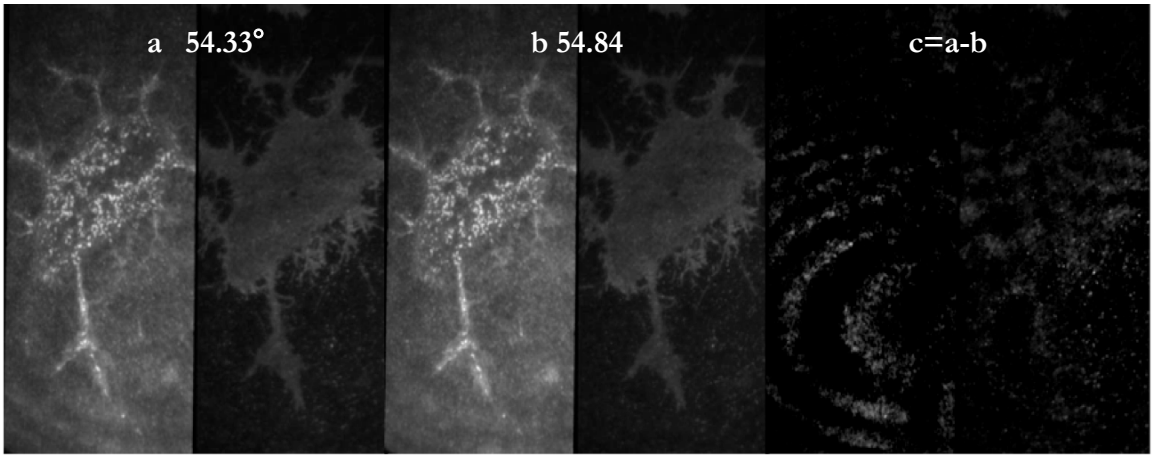

Figure 2.5. Differenced images taken with small changes in incident angle yield little information. The pictures **a** and **b** were captured with at nearly the same incident angle so that there is almost no change in penetration depth. As a result the images are nearly identical and differencing them gives a near-zero result. The three images above are a N2a cell stained with ERTracker green on the left and the membrane localized protein pCS2:lyn-mCherry (20100604 D1 C11b). Image **a** was taken with a 54.33° incident angle. Image **b** was captured at a 54.84° incident angle. Image **c** is the result of subtracting image **b** from image **a**. The impact of changes in the secondary interference pattern is evident.

In finely parsed sequences, the change in image content from one incident angle to another small compared to the change in excitation as the interference pattern is shifted. Subtracting images that differ only slightly exaggerates the variation of excitation due to laser interference. In effect Figure 2.5 demonstrates the magnitude of error seen in many calculations that involve a small difference between two large values.

The ideal solution for eliminating interference fringe variations is to rapidly rotate the excitation beam on the back aperture of the objective. If the image, is taken with a time scale much longer than the rate of rotation, the interference patterns can be nearly completely averaged out.[28] Another solution is to illuminate an annulus on the back aperture rather than at a point. This can be implemented by imaging an optical mask on the back aperture. Neither of these solutions were utilized in this study.

This study instead used the less ideal approach of averaging several (2-5) adjacent images captured at slightly different incident angles. As an example 5 images taken at incident angles 64.3°, 63.5°, 62.9°, 62.3° and 61.6° can be averaged (increments of 10 μm in beam position). The penetration depths of these images vary between 46 and 50 nm. Averaging them significantly suppresses excitation fringe effects without significantly altering the information content.

However there is a limit to how many images can be averaged. Near the maximum angle taking several images causes the loss of very little depth resolution as the change in depth with angle is so small. Referring back to Figure 2.4, we see that the change in penetration depth becomes very large for small angle changes as you approach the critical angle. Therefore averaging must be done over a narrower range of incident angles as the critical angle is approached. In this study five images were averaged near the objective's maximum incident angle. The number of images averaged was reduced to 4, 3 and then 2 as the critical angle was approached. No averaging was done for the images captured closest to the critical angle. Image averaging also has the advantage of further reducing random high frequency noise in the final image. A complete table of the specific images averaged in this study is given in Appendix A.

In future studies angular oversampling could be implemented by finely parsing the incident angle change when sampling (imaging) between the maximum angle of the objective and the critical angle. A running average solution could be implemented for such a dataset to provide far more than the 3 to 5 sections in a 3D image derived for this study. Such a running average could be accomplished by directly averaging adjacent images to yield a long sequence of images with reduced interference effects. Appropriately the images at the ends of this sequence would be minimally processed by this approach.

In this study adjacent images were differenced (subtracted). Doing the same with a finely parsed sequence does not work well as the change in image content from one incident angle to another that is very slightly different, is so small as to exacerbate the impact of error sources such as secondary reflection interference (see Figure 2.5).

Subtracting images using a running difference would provide meaningful information about the distribution of fluorescence concentration in z with a great deal more resolution than in the approach used in this study. As an example images in a sequence with a penetration depth difference of 30 nm could be differenced to result in a sequence of differences with much greater discrimination of fluorescence in z.

2.3 Methods

Total internal reflection fluorescence (TIRF) microscopy. Neuro2a cells cultured in glass-bottom culture dishes were transfected with appropriate plasmids and imaged at 48 h post transfection. TIRF images were obtained using an inverted microscope (Olympus IX71) equipped with an Olympus Apo 100X 1.65 numerical aperture oil objective. eGFP, ER Tracker green and mCherry fluorophores were excited with a 488-nm air-cooled argon laser (P/N IMA101040ALS) and an Optosplit II image splitter (Cairn Research) was used to simultaneously detect fluorescence emission from eGFP and mCherry. Images were aptured with an Andor Technology iXON+ DU-897 back-illuminated EMCCD camera. Data acquisition was accomplished using Andor IQ 1.10.1 software.

The excitation laser incident angle was controlled by an actuated stage with closed-loop controller.[29] Closed-loop control enables reproducible angle of incidence selection with high resolution (specs: 100 nm precision, 3 μm accuracy over the 230 μm TIRF range). The laser alignment and positioning assembly is pictured in Appendix A.

All of the specific incident angle images captured during this study were taken as 64 images sequences. These images were co-added (i.e. are processed to yield an average value z-projection image) to improve signal-to-noise by averaging out rapidly fluctuating noise sources such as shot noise.

Sample exposure rate, percent laser transmission, and gain parameters were initially adjusted for each cell to utilize the full intensity range of the camera while excited by a laser close to the critical angle. Images were acquired beginning at the maximum angle and then sequentially incremented towards the critical angle. The 488 and 561 nm laser lines were linearly s-polarized as revealed using an achromatic 400 to 800 nm 1/2 wave plate (Thorlabs AQWP05M-600).

Cell culture chamber. To reduce the expense of coverslips, I designed a chamber, pictured in Figure 2.6, which is compatible with delicate cell cultures. This chamber itself is fabricated from virgin Teflon. It is sized to match a 35 mm culture dish so that normal culture dish covers can be used. The dish-coverslip junction is sealed via a dry silicon o-ring. As a result the cells are confined in volume that appears, from the health and proliferation of the cells, to have an *in vivo* cytotoxicity comparable to that of commercial culture dishes. This assembly is attached to a stainless steel baseplate via machine screws. The baseplate has a recess sized to hold the 20 mm diameter N-LAF21 coverslips. Screwing the assembly together also provides the force necessary to squeeze the o-ring and thereby to achieve a liquid-tight seal. After some practice, coverslip breakage was reduced

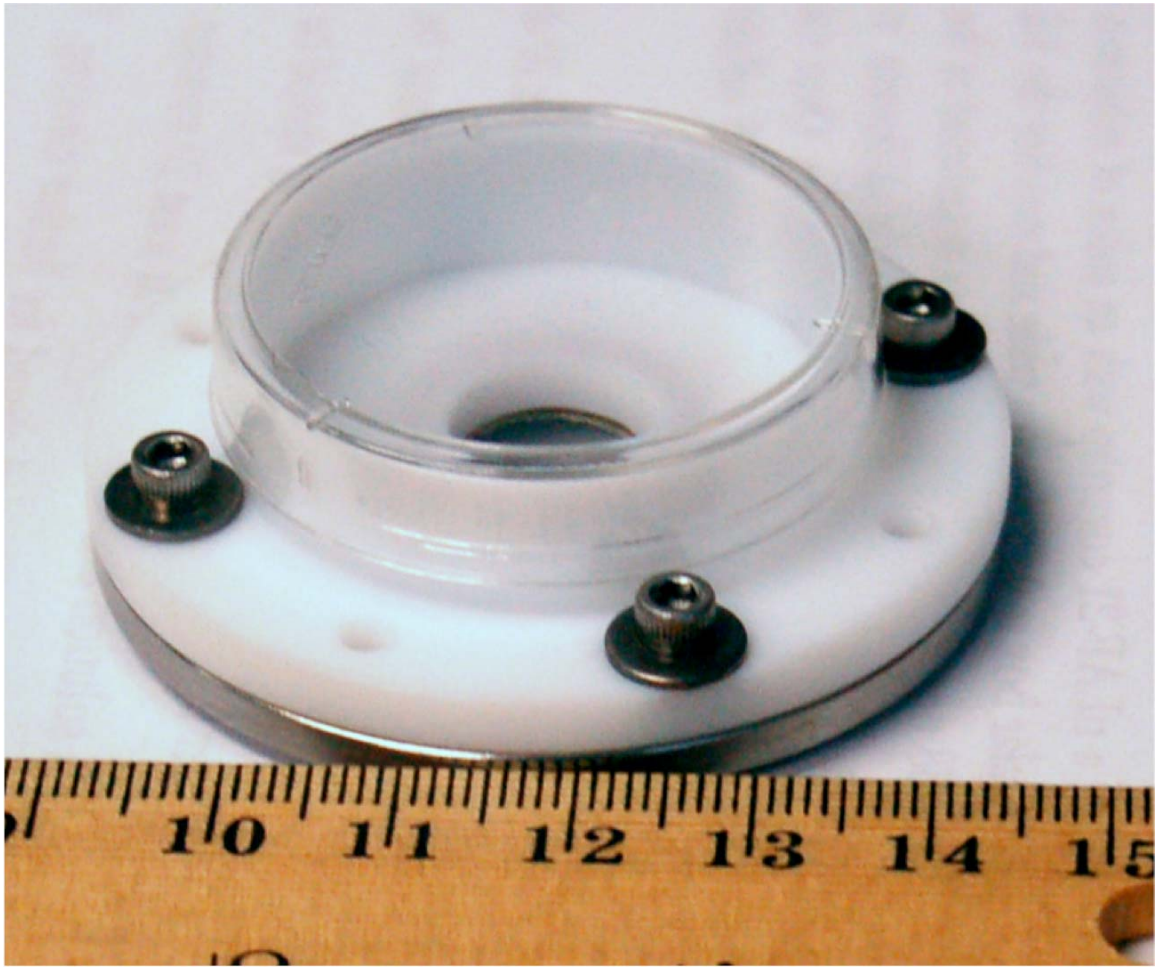

Figure 2.6. A cell culture chamber was fabricated from virgin Teflon that matched the inner and outer diameter, and depth of a commercial 35 mm dish. A silicon o-ring seals the coverslip and chamber so that it is cell media tight. Machine screws are used to assemble this chamber onto a stainless steel baseplate.

to approximately 1 per 20 dishes. The parts, from which the cell culture chamber was assembled, are pictured in Appendix A.

Additionally it should be noted that Delrin was used rather than Teflon in the first version of this chamber. I found that all of the cells died in the dishes fabricated from Delrin. Many variations were explored to try and understand the reason for this without success. Finally new dishes were fabricated from virgin Teflon with the result that the cells thrived. Further literature searches indicate that formaldehyde leaches from Delrin.[30,31]

Stringent cleaning of the culture dish parts is critical. The final assembly must be both sterile and clean of particulate and other contaminates. After use the dishes should be filled with 70% ethyl alcohol or 10% bleach solution and left to sit for at least 20 minutes. Then the dishes should be wiped dry with paper towels and stored for further cleaning. Teflon dishes, baseplates, screws and silicon o-rings are typically cleaned by hand washing in warm, soapy water, followed by 30 minutes sonication in a 2% micro90/DI water solution, followed by extensive rinses in 18 MΩ DI water, followed by 30 minute sonication in acetone in a covered crystallization dish. Then the outside of the crystallization dish containing these parts is very liberally sprayed with 70% ethyl alcohol and it is passed into a sterile tissue culture hood. The parts are individually removed from the acetone dish and blown dry by a high pressure stream of <1μm filtered nitrogen gas. The parts are then stored in a clean, sterile, covered crystallization dish in a sterile tissue culture hood. Assembly is done in the tissue culture hood using sterile tools.

Coverslip cleaning is done separately from the cell culture dish components. The coverslip cleaning protocol is presented in detail in Appendix B. To briefly summarize the procedure: the coverslips are placed in a specially made virgin Teflon carrier, pictured in Figure 2.6, which is in turn is placed in a crystallization dish. The coverslips are sonicated for 20 minutes in a 2% micro90/DI water solution and then rinsed aggressively with DI water. Following this a 2 step RCA cleaning procedure is followed. The first step is to immerse the coverslips in a boiling SC-1 solution (3:2:1 ratio high-purity H2O, 30% NH4OH, 30% H2O2) for 20 min followed by thorough rinsing in 18MΩ DI water. In the

second step the coverslips are immersed in a boiling SC-2 solution (14:3:1 ratio) high-purity water, 30% H2O2, 37% HCl) for 10 minutes followed by stringent rinsing in 18 MΩ water. After rinsing the crystallization dish is refilled with 18 MΩ water, covered, sprayed with 70% ethyl alcohol and stored in a sterile tissue hood. Materials and reagents. Mouse Neuro2a cells (CCL-131) were obtained from American Type Culture Collection (ATCC). Dulbecco's modified Eagle's medium (DMEM) with 4 mM L-glutamine, OptiMEM 1, Leibovitz L-15 imaging medium, ER-Tracker Green and fetal bovine serum (FBS) were purchased from Invitrogen. Expressfect transfection reagent was purchased from Denville Scientific.

Mouse wildtype (wt) α4 and β2 constructs were obtained from Dr. Jerry Stitzel. Mouse α4-eGFP was engineered as previously described.[32] Briefly, eGFP was introduced in frame into the α4 BstEII site with an upstream HA tag after residue 426 in the M3-M4 intracellular loop. eGFP was PCR amplified from the peGFPN1 vector using the forward primer 5'-TTT TGG TCA CCC TAT CCT TAT GAC GTC CCA GAC TAC GCC ATG GTG AGC AAG GGC GAG GAG CTG-3' and the reverse primer 5'-AAAA GGC GTA GTC TGG GAC GTC ATA AGG ATA GG TGA CCT CTT GTA CAG CTC GTC CAT GCC GAG-3'. The PCR product was cut with BstEII and ligated into the *wt* α4 construct to create α4-eGFP. Mutations were introduced into the α4-eGFP and β2-*wt* constructs using the appropriate primers and Quikchange II XL site-directed mutagenesis kit to create the α4L358A-eGFP and the β2-365AAQA368L349M constructs. Plasma membrane reporter, pCS2:lyn-mCherry was obtained from Dr. Scott Fraser. (300 ng per 35-mm dish), to express a red fluorescent protein (pmCherry FP), which is targeted to the plasma membrane. The construct contains two copies of a myristoylation signal sequence subcloned from the Lyn Kinase gene. The signal sequence is immediately upstream of the FP gene and targets the FP to the plasma membrane.

Cell culture and transfections. Mouse Neuro2a cells were cultured using standard tissue culture techniques and maintained in DMEM + 10 % FBS.[33] Plasmid concentrations used for transfection were as follows: 500 ng of each nAChR and GluCl subunit, 75 ng of pCS2:lyn-mCherry. 90,000 cells were plated in the earlier described culture dishes. The following day, plasmid DNA was mixed with cationic lipids by adding appropriate DNA

concentrations to 4 µl of Expressfect transfection reagent in 200 µl DMEM final volume and incubated for 20 min at room temperature to form cationic lipid-DNA complexes. DMEM + DNA-lipid complexes were added to Neuro2a cells in 1 ml of DMEM + 10 % FBS and incubated at 37 ˚C for 4 h, following which, cells were rinsed 2X with DMEM, replaced with 3 ml of DMEM + 10 % FBS and incubated at 37 ˚C for 48 h. For nicotine treatments, a concentration of 0.1 and 1 µM was used for 48 h and 20 min respectively, since these concentrations respectively mimic the nicotine concentrations achieved in smoker's brains in between cigarettes (0.1 µM, 48 h) and during smoking (1µM, 20 min).

2.4 Results

Variable-angle TIRFM is provides the ability to image well-defined layers, or thicknesses, of a cell near a coverslip. By changing the incident angle of the excitation laser we can capture a thinner or thicker optical section. With our current VA-TIRF microscope the thinnest optical section we could image had a ~46 nm penetration depth and the thickest pure TIRF image had a ~250 nm penetration depth.

To test the ability to define layers within the 250 nm closest to the coverslip, we transfected pCS2:lyn-mCherry membrane localized protein into a N2a cell. Just prior to imaging we then stained the cells with ERTracker green. In Figure 2.7**a,** a 46 nm penetration depth image is shown. The mCherry labeled cell membrane is clearly imaged while the darkest part of the ERTracker image is seen in the center of the image where the cell membrane sealed the surface and prevented exposure to the stain. Figure 2.7**a** shows that the cell membrane is imaged in isolation from ER located inside the cell.

To test the ability to isolate deeper cellular organelles we imaged that same cell at two penetrations depths: 240 nm and 80 nm. The 240 and 80 nm images were normalized to account for the change in intensity as a function of incident angle. Then the 80 nm image was subtracted from the 240 nm image to test whether cellular organelles near the membrane could be imaged without interference the plasma membrane. The result is seen in Figure 2.**7b**. The membrane localized mCherry emission is very nearly entirely subtracted out showing that the membrane labeled proteins could be successfully removed.

The ERTracker labeled image in contrast was very bright showing that the ER was well captured up to the ~240 nm penetration depth of that image.

Figures 2.7**a** and **b** together indicated that a cell membrane and ER can be imaged without interference from each other (ie. optically isolated) in living cells.

We then explored whether this would still prove true if a single color was used to image a membrane-bound receptor. To do this we transfected N2a cells with α4 eGFP, β2 wt nicotinic Acetylcholine Receptor (nAChR) subunits and pCS2:lyn-mCherry. In Figure 2.7**c** we see a 46 nm penetration depth image. The mCherry labeled membrane is bright and the α4 eGFP β2 wt nAChR's appear to be uniformly distributed in the membrane with some puncta visible. The 240-80 nm penetration depth image in 7**d** shows that the mCherry labeled membrane is seen at low level while the GFP labeled nAChR α4 subunits are seen in quantity in interior cell organelles.

This experiment was repeated after transfecting a N2a cell with α4 eGFP, β2-365AAQA368L349M nAChR subunits. The mutation in the β2 subunit results in increased transport of nAChRs to the cell membrane. In 7**e** the cell is shown at 46 nm penetration depth. The membrane is clearly seen and evidences labeled nAChRs uniformly across the membrane. There are additionally some small puncta and tubular structures in that image close to the membrane. In 7**f** a 240-80 nm image of the same cell shows extensive ER structure deeper in the cell.

Therefore we conclude that the membrane is significantly isolated from other cellular organelles in the thinnest penetration depth images despite substantial expression of fluorophores located internal to the membrane. We also conclude that the ER and other internal organelles can be imaged with only minor interference from the cell membrane, labeled with the same fluorophores, enabling direct response comparison in future experiments.

Our first goal was to capture a series of VA-TIRFM images that are well discriminated in depth and then to use them to build a 3D image that is representative of the cellular structures within 250 nm of the coverslip. To do this we transfected N2a cells with

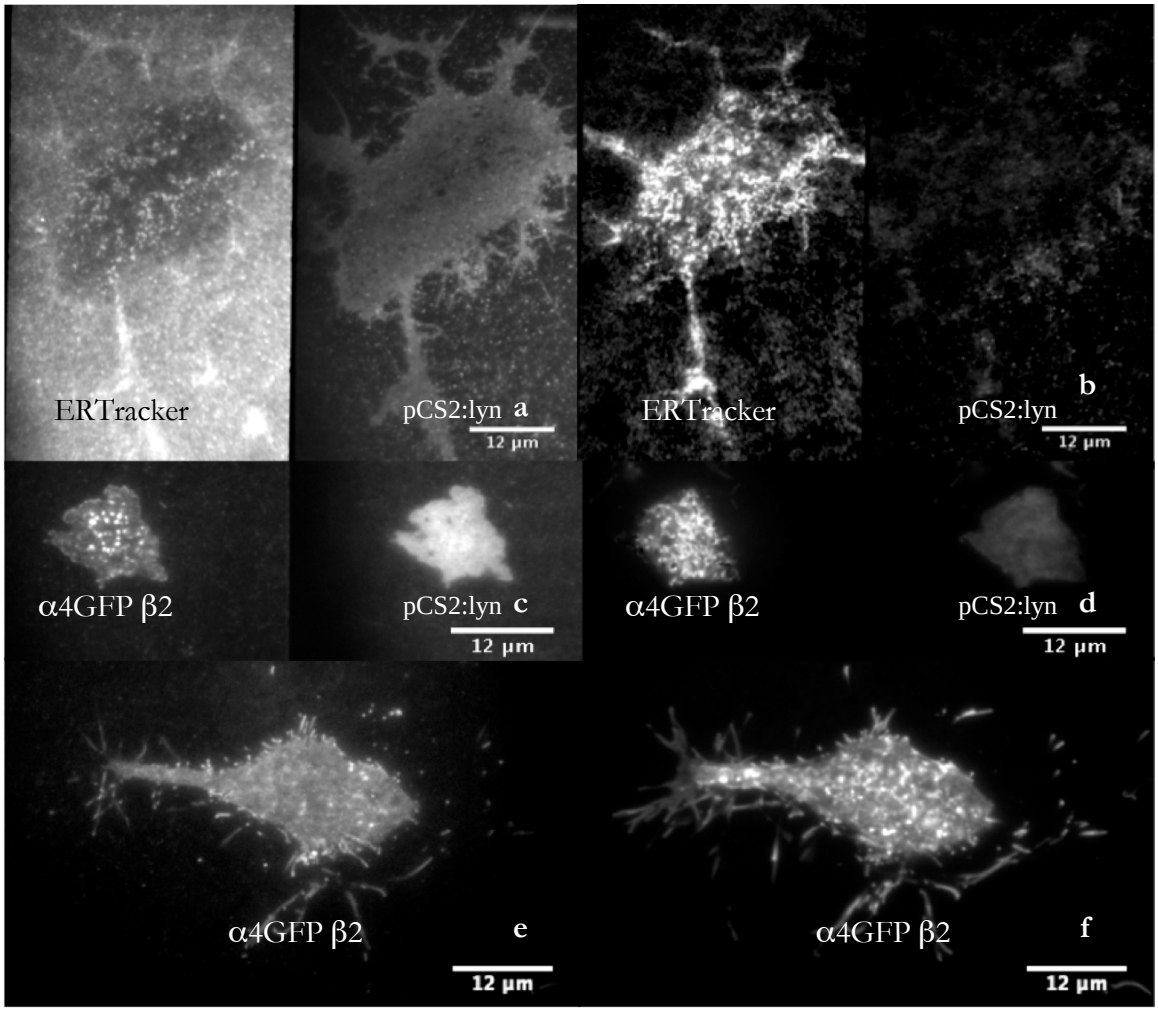

Figure 2.7. A control experiment (**a**) demonstrates that VA-TIRFM is capable of isolating the cell membrane from cell organelles. Additionally it is shown (**b**) that differenced images give information about cell organelles without contamination from membrane signal. Finally it is demonstrated (**c, d, e, f**) that a cell membrane and cell organelles can be imaged in isolation for membrane-expressed proteins labeled with GFP. TIRFM images **a**, **c** and **e** were captured at a penetration depth of 48 nm. TIRFM images **b**, **d**, and **f** are the residual after subtracting an 80 nm penetration depth image from a 240 nm penetration depth image. The 48 nm images are the thinnest which can be captured of a cell using a 1.65 NA objective and a N-LAF21 coverslip. Because these images (**a**, **c**, **e**) are so thin they primarily capture the cell membrane and ER or vesicles that are in contact with, or very close to, the membrane. ~240 nm penetration depth is the deepest that can be captured with this same arrangement and the real beam size of our microscope while remaining in pure TIRF. The residual (**b**, **d**, **e**), after subtracting an 80 nm penetration depth image from a 240 nm penetration depth image, is primarily ER. Images **a** and **b** are control images: the left half of images a and b show ERTracker green stain. Because the cell seals the coverslip from the ERTracker stain the 48 nm image **a** shows a black region where the cell is centered while **b**, the 240-80 nm slice image, shows primarily ER. The right half of images **a**, **b**, **c** and **d** show cells expressing pCS2:lyn-mCherry membrane localized protein. Note that the 48 nm image captured the membrane while very little signal is added in the greater penetration depth images. The cell seen in images **c** and **d** is expressing α4-eGFP β2 wt nAChRs (left) and pCS2:lyn-mCherry (right). The cell in **e** and **f** is expressing α4-eGFP β2-365AAQA368L349M nAChRs (left) and pCS2:lyn-mCherry (right). Camera noise of 110 counts/pixel was subtracted from all of the above images.

α4L358A-eGFP β2 wt nAChR subunits and pCS2:lyn-mCherry. The α4 mutation (L358A)

renders a transport motif inactive. As a result the eGFP labeled subunits accumulate inside the cell. So this experiment, like that seen in 7**a** and **b**, enables us to image the mCherry labeled membrane and eGFP labeled organelles and thereby compare the imaged locations and the fidelity of the 3D model derived from our data.

The imaging results of this experiment are seen in Figure 2.8. On the left is a sequence of VA-TIRFM images taken at 48, 72, 108, 162 and 243 nm penetration depths. These figures capture the total fluorescence within the evanescent field illuminated volume. The mCherry labeled membrane is clearly seen in the 48 nm penetration depth image (top left) and remains approximately the same for the rest of the sequence. In contrast the GFP labeled α4 subunits are more faintly seen in the shallowest image and gain in intensity and structure as the images gain depth. The only processing of these images was camera background subtraction and contrast-brightness adjustment so that they would be visible to the reader.

On the left side of Figure 2.8 are the differenced images defined in Table 5.3 and shown in Figure 2.4. Before differencing, the image intensities of the figures seen on the left are normalized to account for the variation in I(0) as a function of incident angle. The first image in the TIRFM image z-stack is the 46 nm penetration depth image seen in the top right of Figure 2.8. The next down is the difference between the 72 nm image and the 46 nm images. The third down is the difference between the 108 nm and the 72 nm images (2nd and 3rd from the top on the left column). The fourth on the right is the difference between the fourth and the third images (162 nm-108 nm images) on the left. The fifth on the right is the difference between the fifth and the fourth on the left (243 nm-162 nm images). The difference images are the additional fluorescence that is captured each time the incident angle is changed so that a deeper section of the cell is imaged. As such, they approximate the label cellular structure as a function of depth.

The 5 images on the right side of Figure 2.8 were then assembled as a z-stack and converted into a 3D image. The depth was increased by a factor of ~10 (to an apparent 2.5 μm rather than the actual 243 nm) to allow the ER structure to be visible. Because of software limitations the sections are treated as being of equal thickness (500 nm each x 5

layers). Nine views of the resulting 3D image are shown in Figure 2.9. On the top left is an image of the GFP imaged α4 nAChR subunits and next to it is the mCherry labeled membrane. A view of the GFP and mCherry labeled cell 3D model is shown every 22.5° as it is rotated in 8 steps about a vertical axis.

Figures 2.8 and 2.9 together demonstrate that 3D reconstruction captures an appropriately representative thin mCherry labeled membrane, and the much thicker GFP labeled ER and vesicles. Therefore, it appears that VA-TIRFM can be used to create representative 3 D models of cellular structure near the membrane.

We then explored a single label 3D imaging of a membrane embedded protein by transfecting N2a cells with α4-eGFP β2-365AAQA368L349M nAChRs. This β2 mutant increases membrane transport of assembled nAChRs. The cells were also transfected with pCS2:lyn-mCherry membrane localized protein as a control. Similar to what is seen in Figures 2.8 and 2.9 we found that the mCherry labeled membrane image was appropriately represented (not shown).

In Figure 2.10 we see the 3D fluorescence image from the perspective of being in the cell and looking out. The image on the right shows detected fluorescence directly. The image on the left shows a thresholded surface (497 counts per pixel) overlaid on the fluorescence image. The same logarithmic imaging sequence was used to construct this image that was used in Figures 2.8 and 2.9.

In Figure 2.10, the smooth ER and many vesicles are clearly seen. Behind these (closer to the cell surface) the membrane can be seen. In Figures 2.11, 2.12 and 2.13 the 3D model of the cellular structure is further magnified and examined from several angles. As in Figure 2.9, the 5 imaged layers were treated as being equal thickness and magnified by an average factor of ~10. This resulted in an apparent total thickness of 2.5 μm (5 layers, each 500 nm thick in z) as opposed to the actual value of ~243 nm overall.

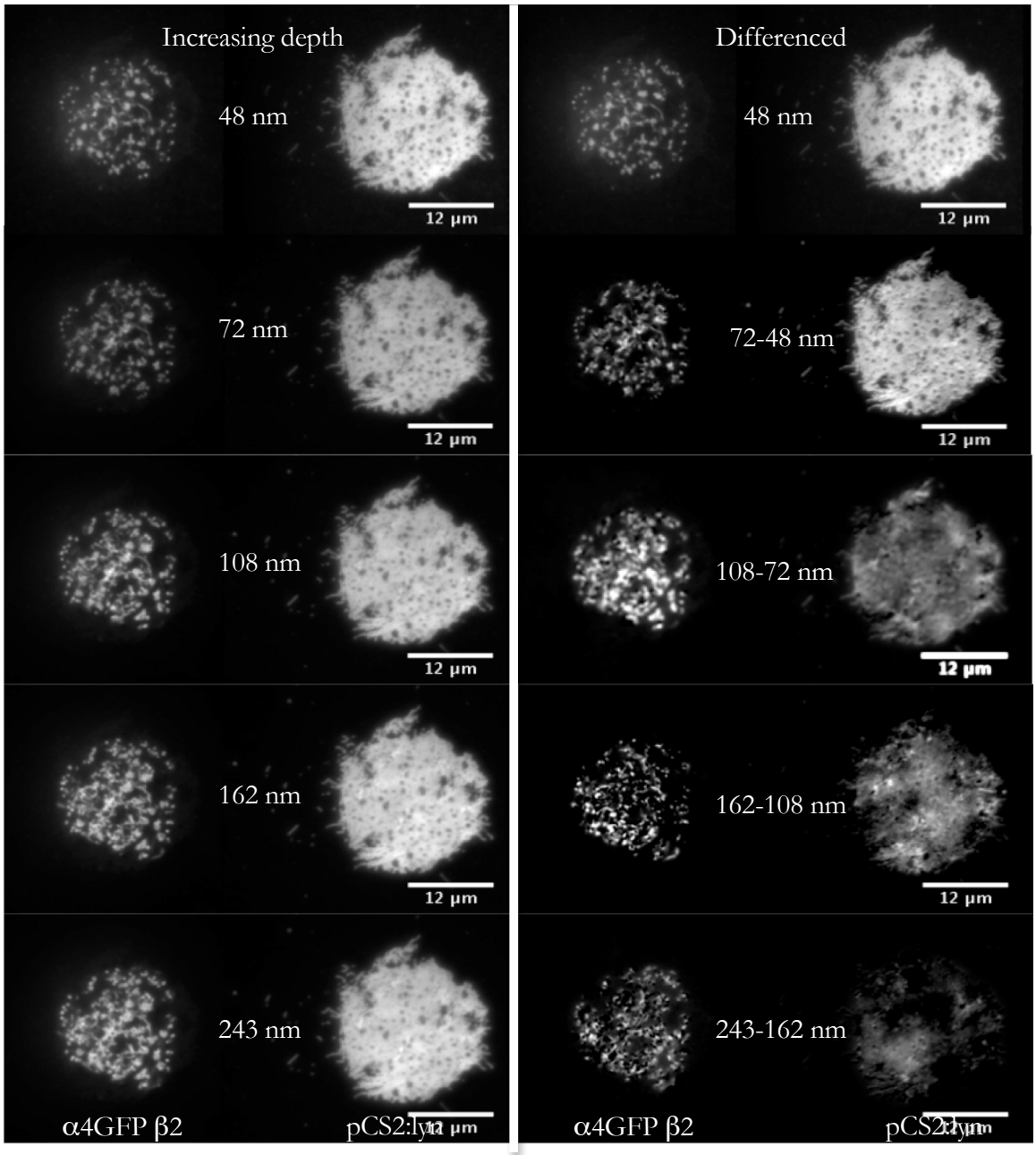

Figure 2.8. A second control experiment demonstrates that a cell membrane and cell organelles can be imaged in isolation. The imaging sequence shown in Figure 2.4 is demonstrated here with a N2a cell. The left column images were captured at penetration depths of 48, 72, 108, 162, and 243 nm (from top to bottom) (Table 5.3). The right column contains the resulting images after differencing (1, 2-1, 3-2, 4-3, 5-4). The differenced images are the additional signal that is captured each time the incident angle is changed to give a thicker image depth The right image in each pair is labeled with pCS2:lyn-mCherry and has the scalebar. The set on the left shows α4L358A-eGFP β2 wt nAChRs. A L358A mutation in the α4 subunit interrupts the transport motif that would normally enable nAChRs to be membrane localized. Therefore this sequence of images provide a side-by-side comparison of the change in signal with increasing penetration depth of an primarily ER localized protein (α4L358A-eGFP on the left) and a membrane localized protein (pCS2:lyn-mCherry on the right).

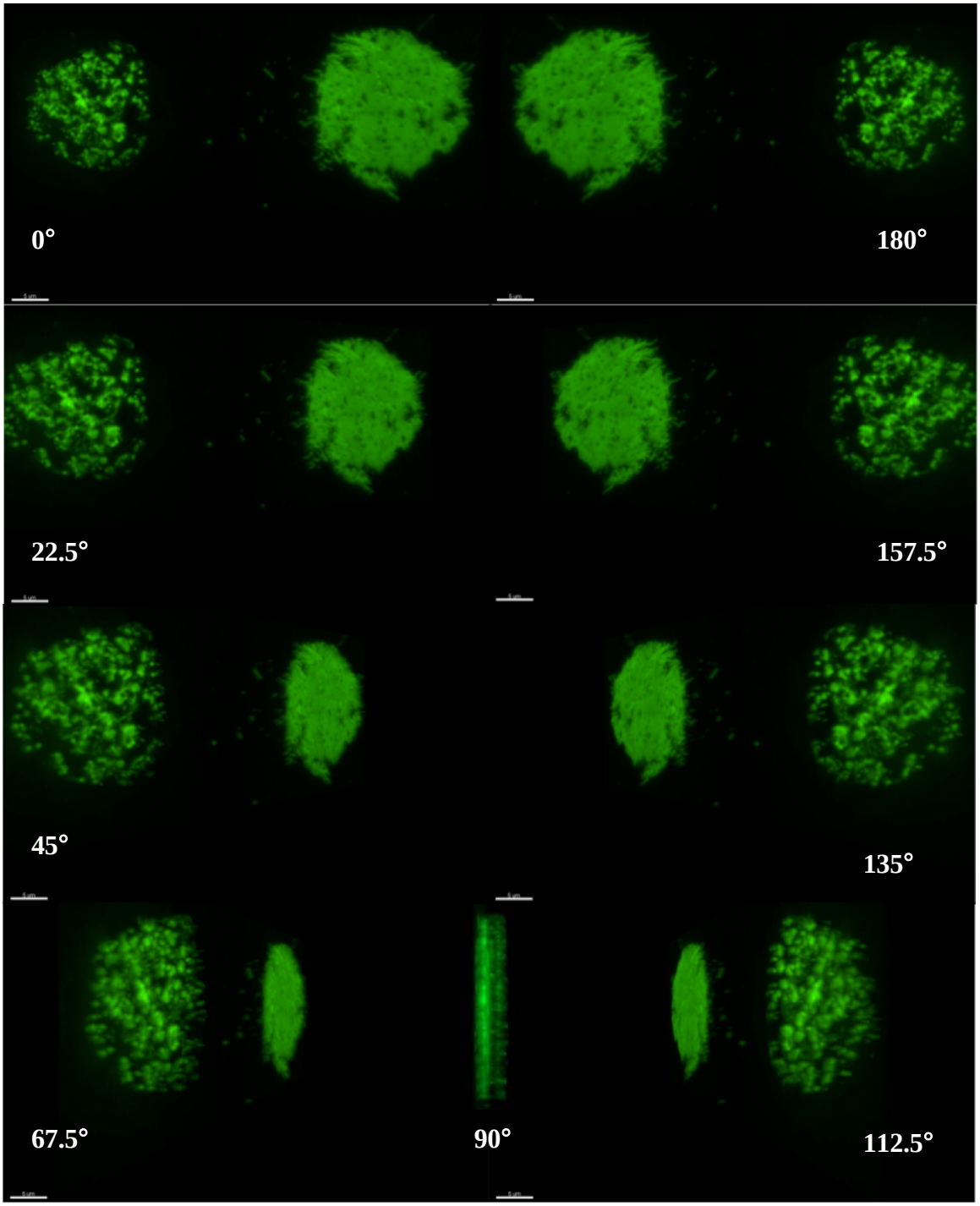

Figure 2.9. A 3D image of a N2a cell is constructed from the differenced images shown in Figure 2.8. Nine views of a three dimensional image are shown being rotated 180° on a central, vertical axis. This 3D image was reconstructed from the five differenced images shown in Figure 2.8 using Imaris software. The scale bar in the bottom left corner of each image is 5 μm long. The total depth of this image was ~240 nm. The z-axis in this figure's images is exaggerated by 10x (expanded to 2.4 microns) for visibility. Magnification in one axis 'stretches' the image such that a normally spherical object becomes cylindrical in appearance (see edge on view in the center bottom). The images were taken face on. The top left perspective is looking out from the center of the cell and the top right from the outside looking in. Each of the successive images is rotated 22.5° from the precious view. Both the GFP labeled nAChRs (outside) and the mCherry labeled membrane (center) are seen.

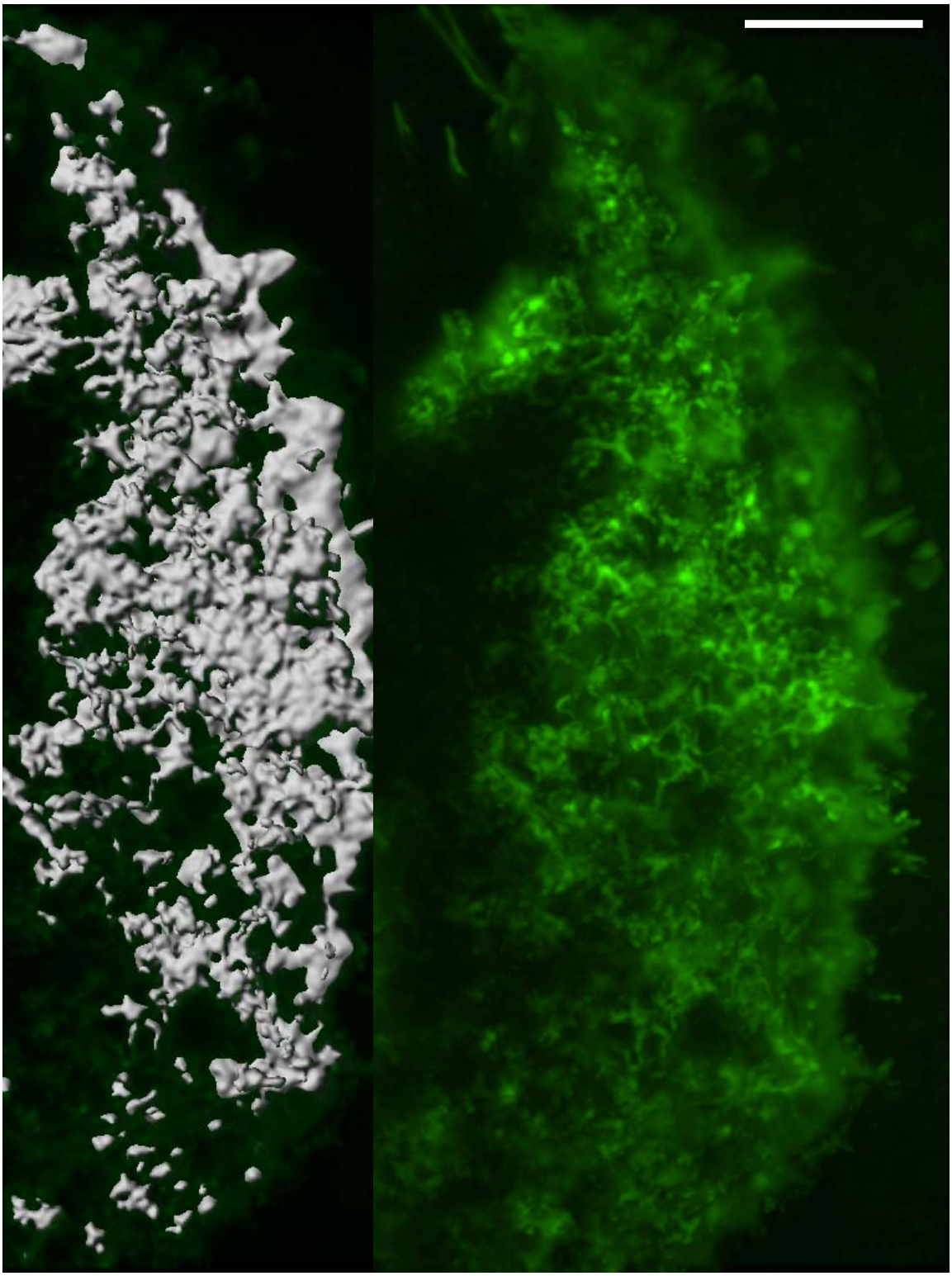

Figure 2.10. A 3D image of cell structures provides information within 250 nm of the membrane with high fidelity. These images show the view from the inside looking out of a 3 D reconstruction that was made from differenced images in using the identical techniques that generated Figure 2.9. On the right, a 240 nm penetration depth TIRFM image is shown of a N2a cell that was transfected with α4-eGFP β2-365AAQA368L349M nAChRs. On the left is a thresholded surface image (497 counts/pixel after background subtraction and normalization) of the same cell. The scale bar at the upper right is 12 μm long.

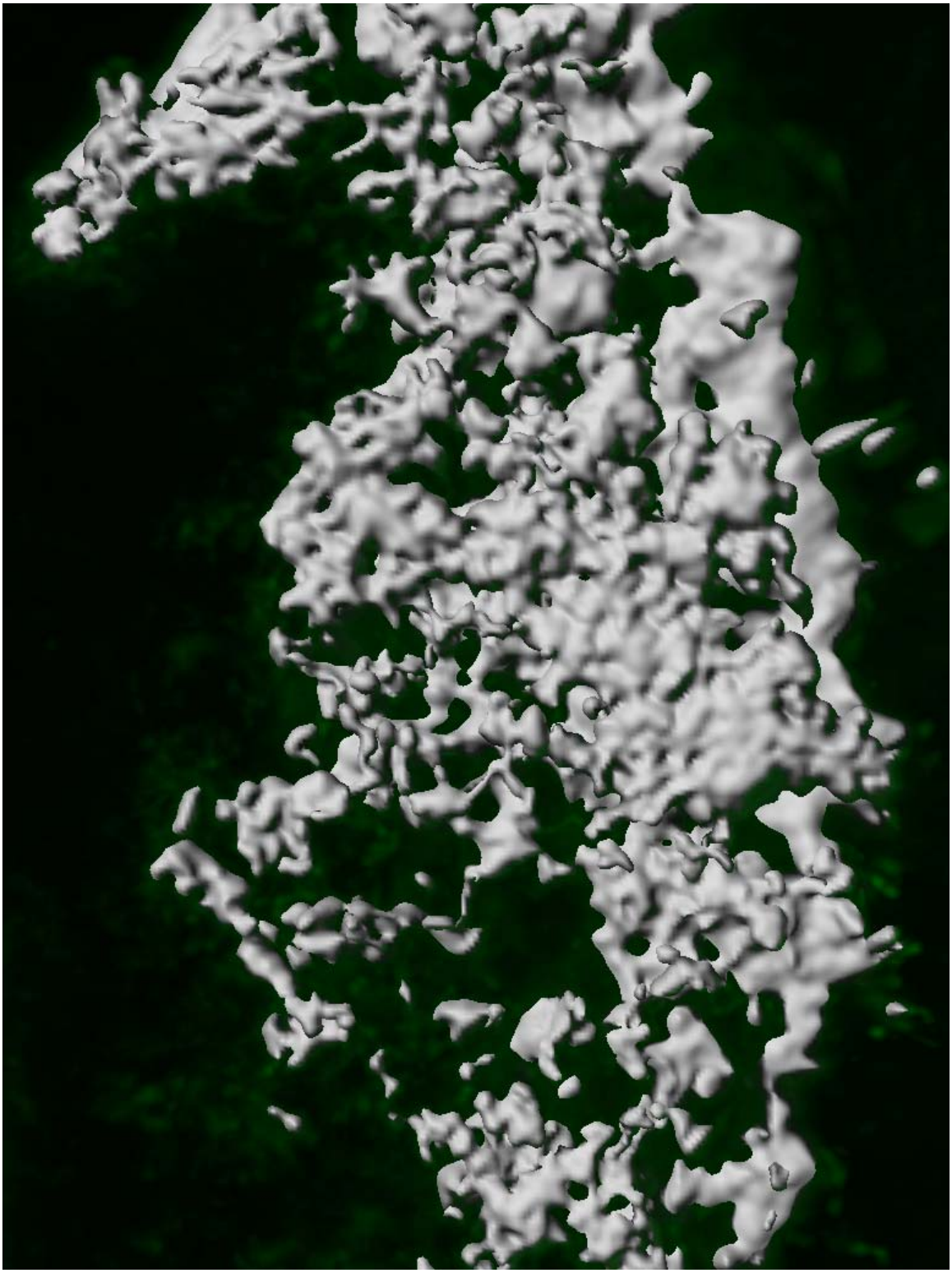

Figure 2.11. A 250 nm thick 3D VA-TIRFM image shows fine structural detail. This view, slightly rotated from that seen in Figure 2.10, implies connections exist between the cell membrane and the smooth ER. In those locations, the separation cannot be resolved by the most shallow TIRM image possible: 46 nm evanescent field penetration depth and 50% illumination at 32 nm. Here the thresholded surface image (identical to Figure 2.10) is overlaid on the green 3 D reconstructed imaged. This view is from the inside looking out. The rotation is on a vertical axis with the left hand side moved (up) out of the page.

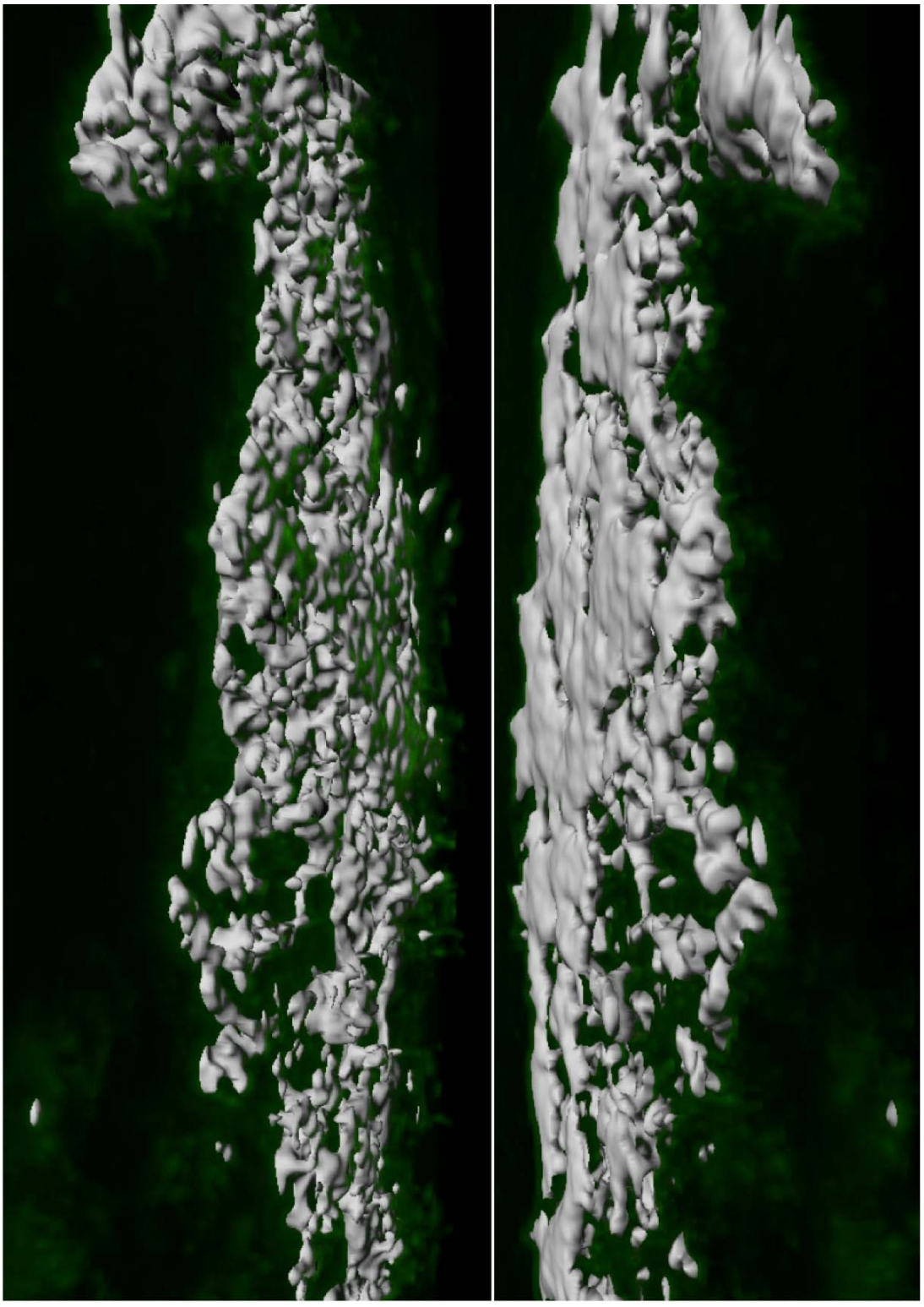

Figure 2.12. Intricate detail is visible indicating that there are many places where parts of the smooth ER are proximate to the membrane such that they cannot be resolved as independent structures. This is the same 3D reconstruction seen in Figures 2.10 and 2.11, of a N2a cell transfected with α4-eGFP β2-365AAQA368L349M nAChRs. The image on the left is further rotated so that the left hand edge seen in Figure 2.10 is nearly perpendicular to the page. The direction of rotation is continued so that the view shows the reconstructed 3D cell image from the membrane side looking in.

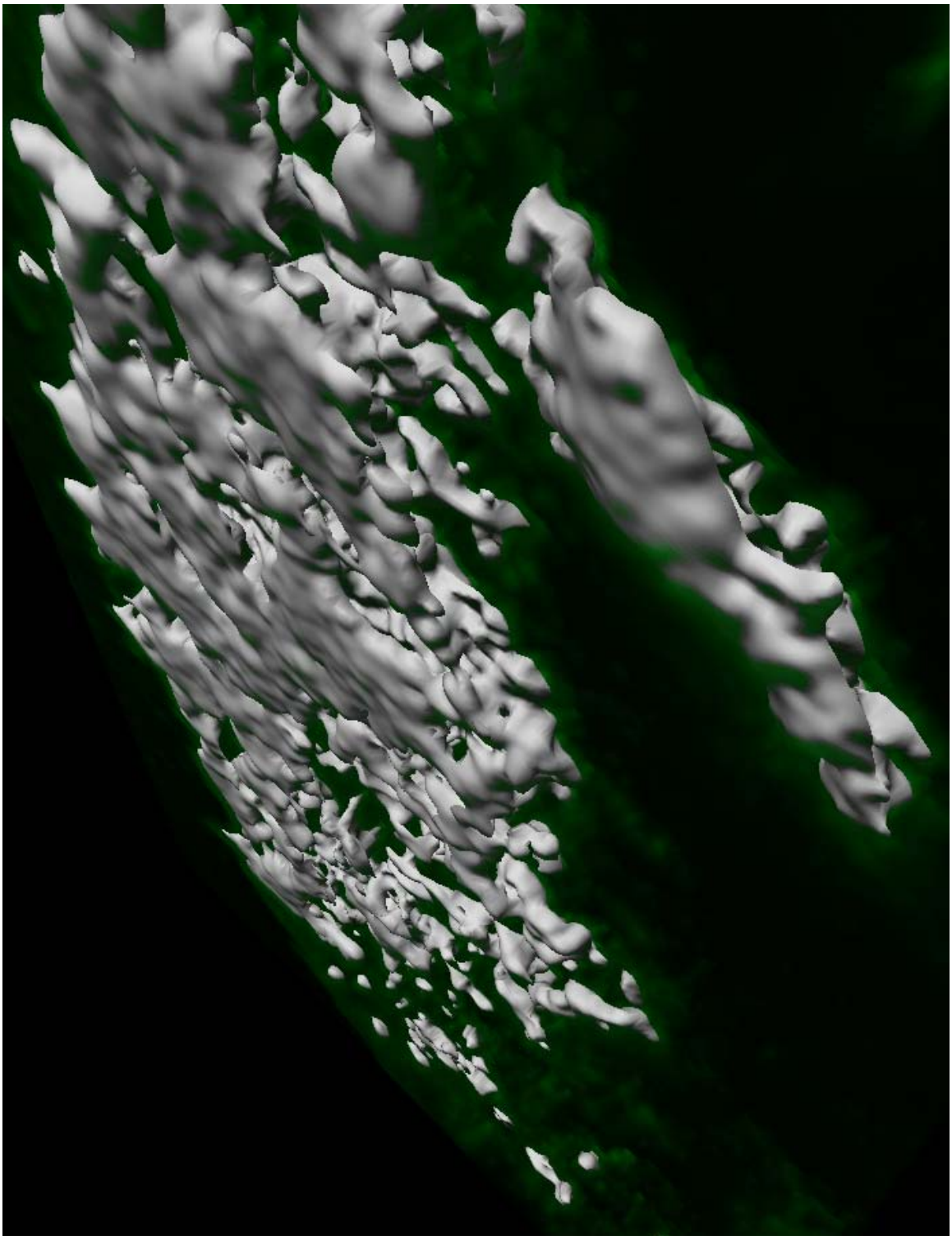

Figure 2.13. Many regions of apparent contact or unresolved proximity between the cell outer membrane and the smooth ER. The rotation of the cell seen in Figures 10, 11, and 12 is continued and the cell is tilted some as well (bottom of the cell rotated into the page). Like Figures 11 and 12 this image too is a combination of thresholded surface and full dynamic range image. This view is from the membrane side of the cell looking in.

A 3D model of a second cell is presented in Figures 2.14 and 2.15. It too is a N2a cell that was transfected with with α4-eGFP β2-365AAQA368L349M nAChRs. As with the other cells, this one was also transfected with pCS2:lyn-mCherry membrane localized protein as a control. Similar to what is seen in Figures 2.8-2.13 we found that the mCherry membrane image was appropriately represented (not shown). The acquisition and processing of this image stack was identical to that used to produce Figures 2.8-2.13. The thresholding surface image was generated at 497 counts per pixel as were those in Figures 2.10-2.13.

The thresholded image too shows a surprisingly complex cellular structure in the 250 nm closest to the coverslip. It also appears that the structure is interconnected. The model indicates sites where the smooth ER either contacts the cell membrane or is sufficiently close that it cannot be resolved as a separate structure.

This raises the question of how unique these features are. In Figure 2.16 three cells are shown. The cells in 2.16**a** and **c** are both transfected with α4-eGFP β2 wt nAChRs. The cell in image 2.16**e** was transfected with α4-eGFP β2-365AAQA368L349M nAChRs and was exposed to 100nM nicotine for 48 hours prior to imaging. Images **a**, **c**, and **e** were taken at 46 nm penetration depth. Images **b**, **d**, and **f** were captured at 200 nm penetration depth. These are full thickness images in that no subtraction was done to localize features. There are bright puncta on the membranes of these three cells.

In image 2.16**b** there are several puncta circled that are located very close to the membrane. In image 2.16**d** it appears that those puncta did not connect to any structure above the membrane. Presumably the puncta imaged in 2.16**b** and 2.16**d** were vesicles. However in the other two cells it appears that puncta did connect to deeper structures. Note that similar features can be seen in Figure 2.7**c** and **e**.

In summary, both α4-eGFP β2 wt and α4-eGFP β2-365AAQA368L349M nAChRs as expressed in N2a cells appear to have junctions where either the smooth ER makes contact with the cell membrane or is so close that it cannot be resolved via TIRFM.

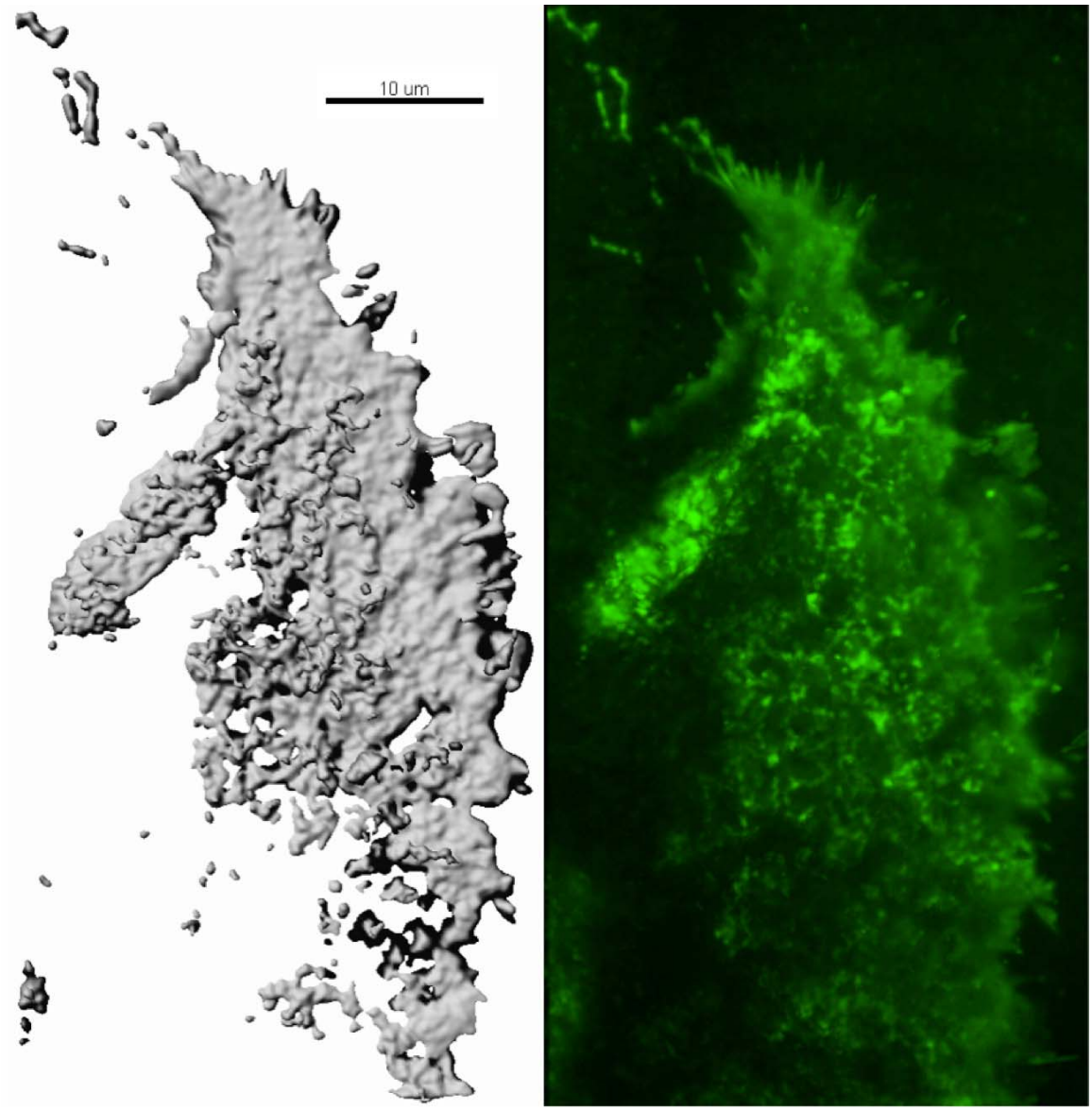

Figure 2.14. A different N2a cell is pictured here with detail shown at a level comparable to that seen in Figures 9-13. On the right, a 240 nm penetration depth TIRFM image is shown of a N2a cell that was transfected with α4-eGFP β2-365AAQA368L349M nAChRs. On the left is a thresholded surface image (497 counts/pixel after background subtraction and normalization) of the same cell. This 3D model was constructed from 5 differenced slices ranging from 46 nm to 240 nm in penetration depth (sequence in Table 5.2).

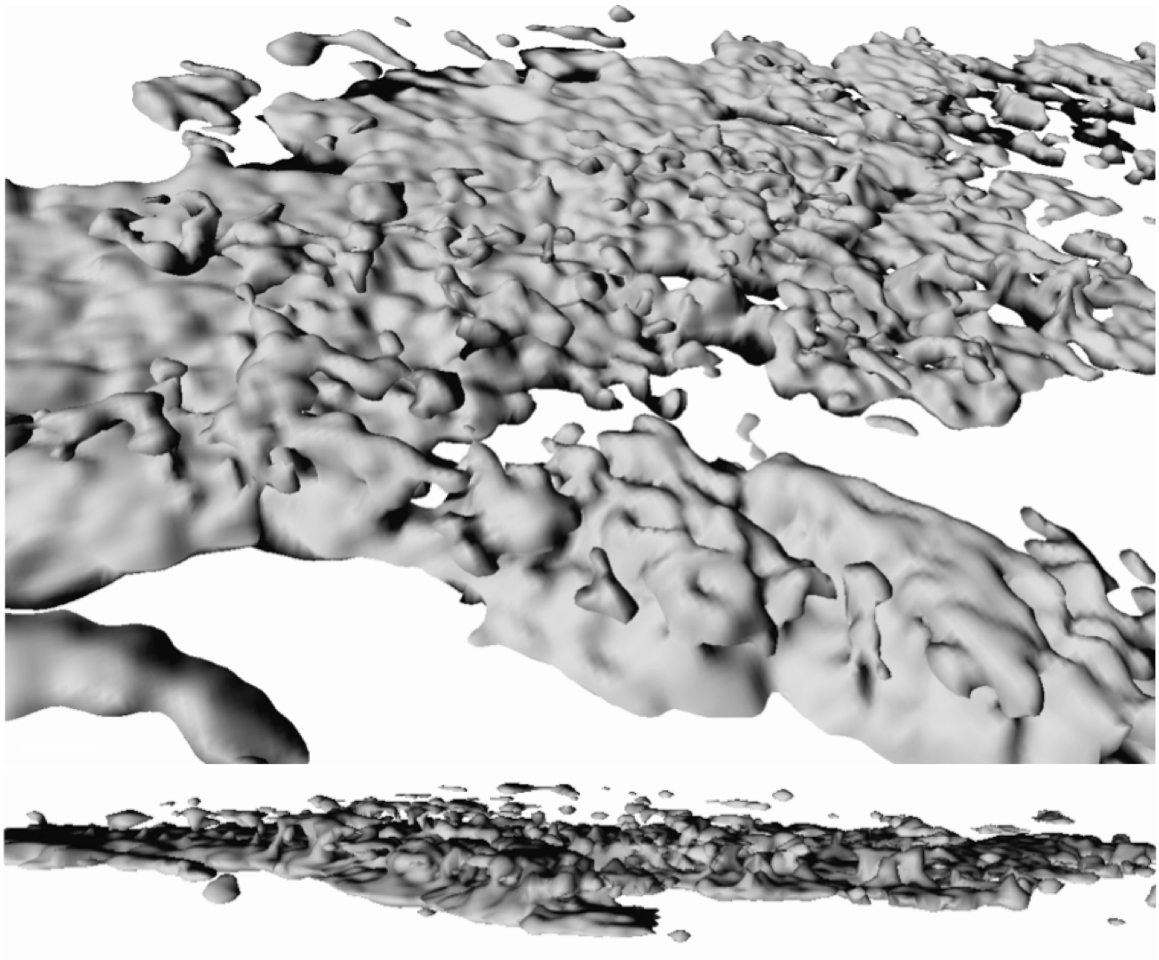

Figure 2.15. Two views are given from the perspective of being on the inside of the cell while looking out. The views above have been rotated ~90 counterclockwise as well as tilted in comparison with the images seen in Figure 2.14. As with the cell in Figures 10-13 there are high intensity regions (>497 counts per pixel after background subtraction) where the isointensity structures shown in threshold surface images seem to indicate either that there is contact between the cell and the smooth ER or alternately that they are so close that they can not be resolved by a 46 nm penetration depth TIRF image.

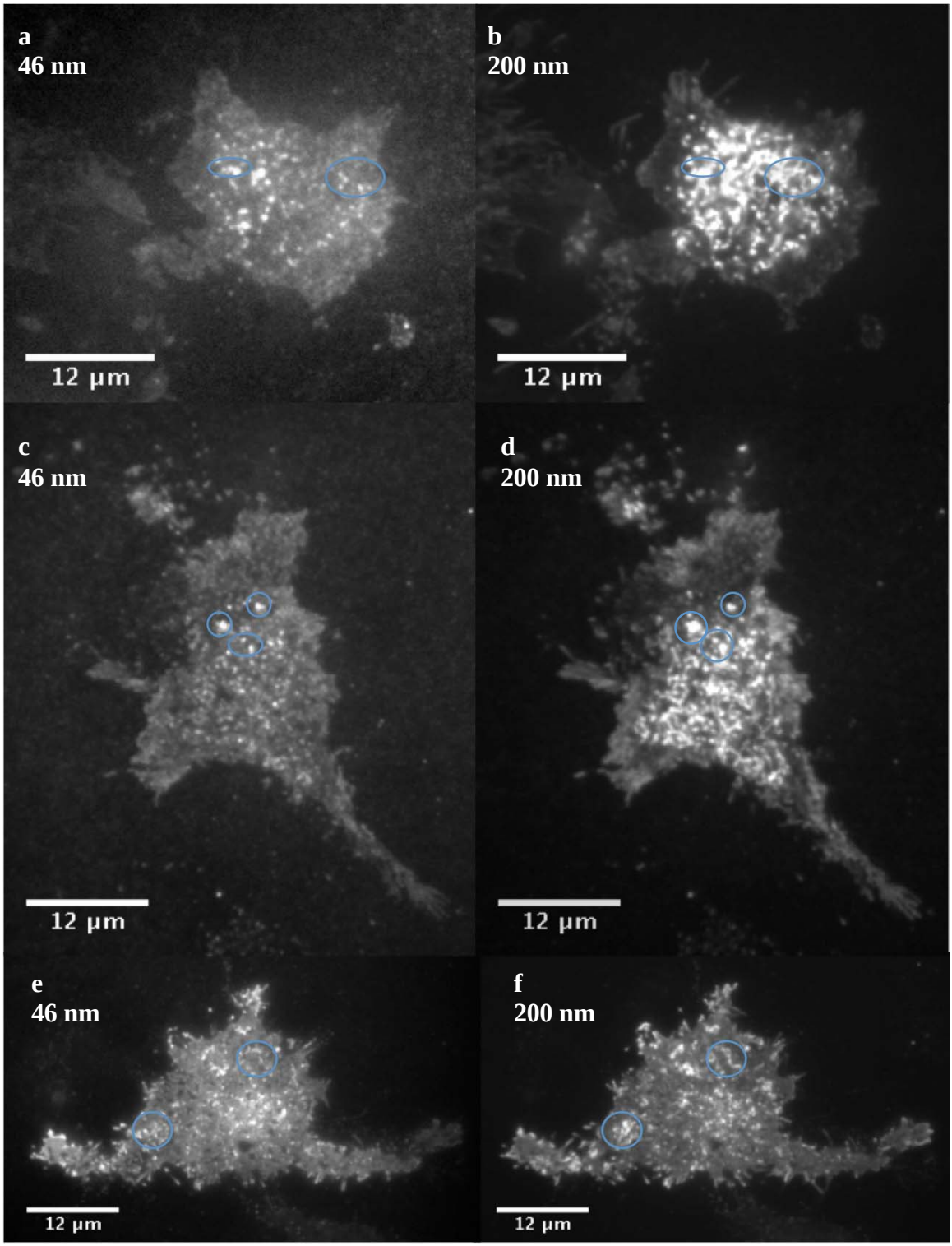

Figure 2.16. Bright nAChR puncta on membrane could be connections between the smooth ER and membrane, localized vesicles (probably the case for circled features in the middle image of this figure) or locations where ER structures are so close to the cell membrane that they cannot be resolved. The left TIRFM images are ~46 nm penetration depth. The right images are approximately 200 nm penetration depth (total power, no differencing). Frequently a bright spot (circled) is seen on the membrane in the thinnest possible TIRF image that appears to be part of a deeper structure. Similar features are seen in nearly all healthy cells with nAChRs that include a membrane transport motif.

2.5 Discussion

It appears that we have detected puncta that may be locations where the smooth ER is in contact with the cell membrane. We know for sure that some detected puncta are so close to the membrane that we cannot detect any separation. How proximate to the membrane are these structures?

The resulting 3D structure is surprisingly detailed. The images indicate that there are direct connections between the membranes and the smooth ER. It appears from this 3D image that these locations are not just self-contained vesicles or invaginations.

In the literature it was reported that smooth ER to cell membrane connections[34,35] have been imaged via electron tomography. Hysashi (ref 34) in particular observed murine neuron cultures with dynamin 1 KO. They observed a great increase in the number of clathrin coated pits in inhibitory synapses and the occurrence of a dynamin 1 independent form of bulk endocytosis. They noted that the observed heterogeneity in the mode of synaptic vesicle recycling in different synapses and function states implied that independent trafficking mechanisms to clathrin mediated endocytosis might exist in normal cells. In addition smooth ER connections with the membranes of other organelles via EM tomography have also been observed.[36]

Therefore it appears plausible that apparent intersections between the smooth ER and outer cell membrane reported here might be real. If so, then VA-TIRFM could be a very useful method for studying the regulatory pathways controlling this potential trafficking mechanism in live cells.

A critical issue with any microscopy technique is: how reliable is this data? Over the index of refraction range of a cell, using a 1.65 objective and N-LAF21 coverslips, a penetration depth of ~46 nm can be achieved. It is critical to remember that the evanescent field decays exponentially. In other words fluorophores near the coverslip surface are more strongly illuminated than those further from the surface. The evanescent field intensity has dropped to ~ 37% at one penetration depth from the surface. Yet even at three times the penetration depth the evanescent field is still ~5% of the intensity at the coverslip surface. Hence an

image taken at a given incident angle, and thereby with a well-defined penetration depth, entangles information from considerably deeper than the penetration depth with that from shallower sections of the cell.

Perhaps the best way to view an individual image is to state that there is a 1-sigma probability that the fluorescence concentration is located within the penetration depth of that image. Therefore the differential technique that was utilized in this VA-TIRFM study optimally yields 3D images in which the fluorophore concentration distribution in z is certain to ~1 sigma.

A 1-sigma certainty is more stringent than the gold standard for defining optical resolution: the Rayleigh criterion.[37] Rayleigh defined a pair of point sources, assuming equal brightness and spectral content, as being resolved when the central diffraction disks are just touching at 50% of maximum. The separation then is equal to the Full Width Half Maximum (FWHM) of one of the beams. 1-sigma certainty is more stringent than the Raleigh criterion as the intensity at that point is only $1/e \approx 37\%$ of maximum rather than at 50%.

The early attempts at VA-TIRFM 3D image reconstruction reported here do not achieve 1-sigma certainty due to non-uniformity of the excitation beam. However they do approach and likely exceed the Rayleigh criterion in terms of vertical resolution. This implies that we have achieved a vertical resolution of <50 nm.

A more rigorous deconvolution of the continuous fluorophore distribution is required to do significantly better than 1-sigma certainty. This could be accomplished via the inverse Laplace transform approach described earlier. An alternate method for disentangling fluorescence that originated at different z distances in an evanescent field would be to use a finite difference technique similar to that used to solve heat transfer and fluid flow problems.

During the course of this study a variety of different imaging strategies were explored. It is clear (see Figure 2.5) that direct differencing very, very finely parsed images is ineffective

as the variation of illumination intensity due to interference patterns is greater than the additional signal detected due to increased penetration depth.

For simple direct differencing with our current microscope we have found that five slices probably represents the most that can be useful. In comparing the efficacy of several approaches we found that five slice z-stacks in general appear to have fewer artifacts than 4, which in turn is better than 3 image z-stacks. Even spaced 5 layer images were constructed and give nearly identical results (not shown) to the 5 slice logarithmic z-stacks. In all cases the 4 slice even space approach gave better results than the 4 slice logarithmic approach. It is not clear to what degree this is due to limitations in the image processing software.

Image fidelity or goodness was here evaluated in a fashion similar to that used when evaluating AFM images: by how sharply defined features are and by an absence of artifacts. Here we define artifacts as repeated structures across an image. As an example, an artifact in a reconstructed image could be identified if the visualized structures have relatively round, twisted shapes throughout most of a cells were connected in one, cell-wide, section with a parallel set of cylindrical or conical features. So the images were examined for features or associations that were repeated as patterns to identify artifacts as would be done when evaluating AFM images.

This kind of artifact is certain to occur when the image is stretched in z (by 10 x in the case of the papers presented herein). It is also likely to occur when the collected image stack has significantly varying thicknesses. Every image processing software package identified, including ImageJ and Imaris 7.0, reconstruct images assuming that every image in the stack is of equal thickness. If on slice is twice as thick as another the final result will be to artificially stretch or compress those regions in a 3D reconstruction. Therefore it is logical to prefer even spaced (in penetration depth) differenced images when doing 3 D image reconstructions.

As shown earlier (e.g. Figure 2.4) even spaced differential images are limited to a z-stack containing only five slices of ~50 nm thickness (each). Clearly it would be beneficial to get

finer z resolution than this. Alternative approaches would include interleaving images so that two stacks of 50 nm thick images could be offset by 25 nm.

While continuous 3D image reconstruction is a challenging problem, there are clear first steps that can be taken by future researchers. Three major impediments remain to be solved for significantly finer z resolution:

1. Image processing software in which the z value of each image in a stack can be individually set and

2. A substantial reduction in excitation laser interference pattern. The first ways to achieve that are to improve the index of refraction match between the coverslip and the immersion oil and to replace the optics that guide the excitation laser with ones that have high quality antireflection coatings. If that is not sufficient, two methods for ensuring elimination of interference patterns are spinning beam and annular mask. With spinning beam the radius must be increased or decreased to change angle of incidence. Precise control of this is possible but will require some though and very good optical alignment. VA-TIRFM with an annular mask is tougher. Perhaps the image of the mask on the objective back plane could be expanded or contracted optically (in analogy to a zoom lens).

3. A smaller excitation laser beam focal spot would significantly reduce the variation in incident angle across the beam. Therefore more finely parsed images could be taken. A factor of two to three reduction in beam size would be sufficient to enable 10 differential slices to be acquired rather than the current limit of 5.

Summary

We have demonstrated that TIRFM using a 1.65 NA objective enables cellular membranes to be imaged in near isolation from the interior of a cell. Further, by using a close-loop controlled positioner, the incident angle of the excitation laser can be repeatably set. This in turn enables images to be captured with known and controlled evanescent field penetration depths. We have shown that the deepest pure TIRF image that can be taken, even with a 1.65 NA objective and high index N-LAF21 coverslips, is about 250 nm thick.

A novel, and relatively simple image processing technique was developed during this study wherein several images are taken with known penetration depths. By normalizing these images, to account for the change in evanescent field intensity as a function of incident angle, they can be directly subtracted to yield difference images in which cellular structures can be optically isolated to distances within 46 nm of the coverslip surface and thereafter at defined distances up to ~250 nm.

We have also demonstrated that these differenced images can be used to construct detailed cellular structure models of up to 250 nm depth. In doing so it appears that cellular organelles can be located vertically to within ~50 nm at present and with higher precision given further development.

Finally we have detected puncta where the smooth ER may intersect with the cell membrane presumably for the purposes of rapid transport of lipids and membrane bound proteins including nAChRs. Such tubular connections between the ER and outer membrane could represent an alternate trafficking mechanism to transport via discrete vesicles. VA-TIRFM appears to be well suited for investigating mechanisms controlling the assembly of functional receptors or lipid rafts in living cells via pulse-chase experiments.

In conclusion, we confidently expect that VA-TIRFM will provide insight into trafficking mechanisms by enabling imaging of cell membranes discrete from images of nearby cellular components.

Acknowledgements

Thanks to Joe Shepherd, Dan Axelrod, Rahul Srinvasan, Chris Richards, and Henry Lester. I could never have hoped to complete this VA-TIRFM study without the skilled work and kind help of Mike Roy and Steve Olson of the Chemistry Department's Instrument shop.

Caltech Dean Grad Studies/Provost, NS11766, Louis and Janet Fletcher, and The Michael J. Fox Foundation are gratefully thanked for funding.

References

[1] Axelrod, D. Cell-substrate contacts illuminated by total internal reflection fluorescence, J Cell Bio, (1981) **89** 141-145.

[2] Lanni, F., Waggoner, A.S. and Taylor, D.L., Structural organization of interphase 3T3 fibroblasts studied by total internal fluorescence microscopy, J Cell Bio, (1985) **100** 1091-1102.

[3] Olveczky, B.P., Periasamy, N. and Verkman, A.S., Mapping fluorophore distributions in three dimensions by quantitative multiple angle-total internal reflection fluorescence microscopy, Biophysical J (1997) **73** 2836-2847.

[4] Stock, K. et al., Variable-angle total internal reflection fluorescence microscopy (VA-TIRFM): realization and application of a compact illumination device, J Micro, (2003) **211** 19-29.

[5] van't Hoff, M, de Sars, V. and Oheim, M., A programmable light engine for quantitative single molecule TIRF and HILO imaging, Opt Express (2008) **16** 18495.

[6] Steyer, J.A. and Almers, W., Tracking single secretory granules in live chromaffin cells by evanescent-field fluorescence microscopy, Biophys J (1999) **76** 2262-2271.

[7] Loerke, D., Preitz, B., Stuhmer, W. and Oheim, M., Super-resolution measurements with evanescent fluorescence excitation using variable beam incidence, J Biomed Opt (2000) **5** 23-30.

[8] Loerke, D., Stuhmer, W. and Oheim, M., Quantifying axial secretory-granual motion with variable-angle evanescent-field excitation, J Neurosci Meth (2002) **119** 65-73.

[9] Reichert, W.M., Suci, P.A., Ives, J.T. and Andrade, J.D., Evanescent detection of adsorbed protein concentration-distance profiles: fit of simple models to variable-angle total internal reflection fluorescence data, Appl Spec (1987) **87** 503-508.

[10] Rangnekar, V.M. and Oldham, P.B., Investigation of the microenvironment polarity of a chromatographic surface using total internal reflection fluorescence, Anal Chem (1990) **62** 114-1147.

[11] Toriumi, M., Saito, S., Kawaguchi, K. and Aiki, K., Variable-angle ultraviolet total-internal-reflection fluorescence spectroscopy using a white excitation light source, Rev. Sci. Instrum (1995) **66** 3520-3526.

[12] van't Hoff, M., Reuter, M., Dryden, D.T.F. and Oheim, M., Screening by imaging: scaling up single-DNA-molecule analysis with a novel parabolic VA-TIRF reflector and noise-reduction techniques, Phys. Chem. Chem. Phys., (2009) **11** 7713-7720.

[13] Lue, N. et al., Live cell refractometry using microfluidic devices, Optics Lett. (2006) **31** 2759-2761.

[14] Maier, J., Walker, S., Fantini, S., Franceschini, S. and Gratton E., Possible correlation between blood glucose concentration and the reduced scattering coefficient of tissues in the near infrared, Opt. Lett. (1994) **19,** 2062–2064.

[15] Brunsting, A. and Mullaney, P., Differential light scattering from spherical mammalian cells, Biophys. J. (1974) **14** 439–453.

[16] Brunsting, A. and Mullaney, P., Differential light scattering from spherical mammalian cells, Biophys. J. (1974) **14** 439–453.

[17] Beuthan, J., Minet, O., Helfman, J. and Muller, G., The spatial variation of the refractive index in biological cells, *Physics in Medicine and Biology*, (1996) **41**, 369-382.

[18] Beuthan, J., Minet, O., Helfman, J. and Muller, G., The spatial variation of the refractive index in biological cells, *Physics in Medicine and Biology*, (1996) **41**, 369-382.

[19] Wilson, J.D., Cottrell, W.J. and Foster, T.H., Index-of-refraction-dependent subcellular light scattering observed with organelle-specific dyes, J Biomed Optics (2007) **12** 014010.

[20] Vitkin, I., Woolsey, J., Wilson, B., and Anderson, R., Optical and thermal characterization of natural (sepia oficinalis) melanin, Photochem. Photobio. **59** 455–462.

[21] Schott glass N-LAF21: http://refractiveindex.info/?group=SCHOTT&material=N-LAF21.

[22] Reichert, W.M., Suci, P.A., Ives, J.T. and Andrade, J.D., Evanescent detection of adsorbed protein concentration-distance profiles: fit of simple models to variable-angle total internal reflection fluorescence data, Appl Spec (1987) **87** 503-508.

[23] Rangnekar, V.M. and Oldham, P.B., Investigation of the microenvironment polarity of a chromatographic surface using total internal reflection fluorescence, Anal Chem (1990) **62** 114-1147.

[24] Olveczky, B.P., Periasamy, N. and Verkman, A.S., Mapping fluorophore distributions in three dimensions by quantitative multiple angle-total internal reflection fluorescence microscopy, Biophysical J (1997) **73** 2836-2847.

[25] Hellen, E.H. and Axelrod, D., Fluorescence emission at dielectric and metal-film interfaces, J.Opt Soc Am B (1987) **4**, 337-350.

[26] ImageJ v1.44c is supported by the National Institute of Health. It can be downloaded at: http://rsbweb.nih.gov/ij/

[27] Bitplane Scientific Software: http://www.bitplane.com/

[28] Mattheyses, A.L., Shaw, K. and Axelrod, D., Effective elimination of laser interference fringing in fluorescence microscopy by spinning azimuthal incidence angle, Microsc. Res. Tech. (2006) **69** 642-647.

[29] Thorlabs pn PT1Z8 motorized translation stage with pn TDC001 T-cube DC motor controller. Thorlabs, 435 Route 206 North, Newton, NJ 07860, USA.

[30] LaIuppa, J.A., McAdams, T.A., Papoutsakis, E.T. and Miller, W.M., Culture materials affect ex vivo expansion of hematopoietic progenitor cells, JBiomedMatlsRes (1997) **36** 347-359.

[31] Ata, S.O. and Yavuzyilmaz, H., In vitro comparison of the cytotoxicity of acetal resin, polymerized resin and auto-polymerized resin as denture base materials, JBiomedMatlsRes PtB (2009) **91B** 905-909.

[32] Nashmi, R., Dickinson, M.E., McKinney, S., Jareb, M., Labarca, C, Fraser, S.E., Lester, H.A., Assembly of $\alpha_4\beta_2$ nicotinic acetylcholine receptors assessed with functional fluorescently labeled subunits: effects of localization, trafficking, and nicotine-induced upregulation in clonal mammalian cells and in cultured midbrain neurons. J Neurosci (2003) **23** 11554-11567.

[33] Son, C.D., Moss, F.J., Cohen, B.N., and Lester, H.A., Nicotine normalizes intracellular subunit stoichiometry of nicotinic receptors carrying mutations linked to autosomal dominant nocturnal frontal lobe epilepsy, Mol Pharmacol (2009) 75 1137-1148.

[34] Spacek, J. and Harris, K.M., Three-Dimensional Organization of Smooth Endoplasmic Reticulum in Hippocampal CA1 Dendrites and Dendritic Spines of the Immature and Mature Rat, J Neurosci (1997) **17** 190-203.

[35] Hayashi, M., et al., Cell- and stimulus-dependent heterogeneity of synaptic vesicle endocytic recycling mechanisms revealed by studies of dynamin 1-null neurons, PNAS (2008) 105 2175-2180.

[36] Yla-Anttila, P., Vihinen, H., Jokitalo, E. and Eskelinen, E.L., 3D tomography reveals connections between the phagophore and endoplasmic reticulum, Autophagy (2009) 1180-1185.

[37] Strutt, J.W., Investigations in optics, with special reference to the spectroscope, Philosophical Magazin, (1879) 8 261-274, 403-411, 477-486 and (1880) 9 40-55.